microbial cell

Research Article

www.microbialcell.com

Yippee-like protein Moh1 links gene expression to metabolism and selective stress resistance in *Saccharomyces cerevisiae*

Çağla Ece Olgun[1,a], Gizem Turan Duman[1,a], Gizem Güpür[1], Hamit İzgi[1], Mariam Huda[2], Demet Çetin[3], Zekiye Suludere[4], Fatma Küçük Baloğlu[5], Ayşe Koca Çaydaşı[2,*] and Mesut Muyan[1,*]

[1] Department of Biological Sciences, Middle East Technical University, 06800, Çankaya-Ankara, Türkiye.
[2] Department of Molecular Biology and Genetics, Koç University, Istanbul, Türkiye.
[3] Department of Mathematics and Science Education, Gazi Faculty of Education, Gazi University, 06500, Ankara, Türkiye.
[4] Department of Biology, Faculty of Science, Gazi University, 06500, Ankara, Türkiye.
[5] Department of Biology, Giresun University, Giresun, Türkiye.

[a] Equal contribution: Should be considered as the first author.
* Corresponding authors:
Ayşe Koca Çaydaşı, E-mail: aykoca@ku.edu.tr;
Mesut Muyan, E-mail: mmuyan@metu.edu.tr

ABSTRACT The Yippee-like (YPEL) proteins are a evolutionarily conserved eukaryotic family implicated in proliferation, senescence, and stress adaptation, yet their molecular functions remain poorly defined. Humans possess five paralogs (YPEL1–YPEL5), while the budding yeast *S. cerevisiae* contains a single ortholog, *MOH1*, previously linked to stress responses but with an unclear cellular role. Here, we investigated the function of *MOH1* in *S. cerevisiae*. *MOH1* deletion resulted in stress-specific phenotypes, including increased sensitivity to sodium azide and sulfuric acid, but enhanced resistance to hydrogen peroxide and acetic acid. Moh1 protein levels were dynamically regulated, decreasing upon hydrogen peroxide treatment and increasing in response to sulfuric acid. Morphological analyses including SEM revealed that *moh1Δ* cells are rounder, form aggregates, and exhibit altered surface architecture independently of stress. RNA profiling and FTIR spectroscopy uncovered transcriptional reprogramming and metabolic remodeling, including alterations in lipid, protein, and cell wall polysaccharide levels and composition. Functional analyses showed that increased resistance to hydrogen peroxide is not due to altered mitochondrial ROS production but rather to reduced intracellular ROS accumulation. This effect is attributed to decreased cellular uptake resulting from altered permeability, supported by resistance to Congo red and sensitivity to SDS, consistent with cell envelope remodeling. Collectively, our findings identify Moh1 as a regulatory factor linking gene expression to metabolism and cellular architecture, thereby influencing cell envelope permeability and conferring selective stress resistance in *S. cerevisiae*.

doi: 10.15698/mic2026.06.881
Received originally: 12.11.2025;
in revised form: 28.04.2026,
Accepted: 18.05.2026,
Published: 29.06.2026.

Keywords: *MOH1*, *S. cerevisiae*, stress response, SEM, RNA-Seq, FTIR.

Abbreviations:
AMA - Antimycin A,
DEG - Differentially Expressed Gene,
E2 - 17β-Estradiol,
ER - Estrogen Receptor,
FTIR - Fourier Transform Infrared Spectroscopy,
GO - Gene Ontology,
H_2DCFDA - 2′,7′-Dichlorodihydrofluorescein Diacetate,
HCA - Hierarchical Cluster Analysis,
moh1Δ - MOH1 Deleted,
PCA - Principal Component Analysis,
ROS - Reactive Oxygen Species,
RNA-Seq - RNA Sequencing,
RT-qPCR - Reverse Transcription Quantitative Polymerase Chain Reaction,
SEM - Scanning Electron Microscopy,
SGD - Saccharomyces Genome Database,
WB - Western Blot,
WT - Wild Type,
YPD - Yeast Extract Peptone Dextrose,
YPEL - Yippee-Like Protein,
YPRG - Yeast Extract Peptone Raffinose Galactose.

INTRODUCTION

The *YPEL* family has 100 genes in 68 species, ranging from yeast and plants to mammals, with a remarkably high nucleotide sequence identity [1–3]. While the budding yeast *Saccharomyces cerevisiae* (*S. cerevisiae*) contains a single gene named MOH1 (YBL049W), the human *YPEL* family includes five YPEL genes, *YPEL1-5*, located on different chromosomes, which are suggested to have arisen from ancestral gene duplications [1–3]. The YPEL2, YPEL3, and YPEL5 genes are ubiquitously expressed, albeit at varying levels, in human tissues; whereas, *YPEL1* and *YPEL4* show expression patterns largely restricted to the testis and brain, respectively [2]. In addition to the ubiquitous tissue expressions, various signaling pathways, including 17β-estradiol (E2)-estrogen receptor (ER) signaling [4, 5], co-modulate the expressions of *YPEL2, YPEL3*, and *YPEL5*.

The YPEL family genes encode small proteins with a high amino-acid sequence identity predicted to form a zinc-finger-like metal binding pocket, or the Yippee domain [1, 2]. This high degree of sequence identity among YPEL proteins results in structural conservation that is likely reflected in functional commonalities, as YPEL proteins are involved in similar cellular processes, ranging from proliferation, senescence, and death [3, 4, 6–22]. Consistent with these, deregulated YPEL gene expressions have been suggested to be associated with the initiation and/or development of various disorders, malignancies, and resistance to therapies [6, 12, 13, 20, 23–29].

Despite the potential importance of YPEL proteins in physiology and pathophysiology, the evolutionary conservation in nucleotide sequences, the ubiquity, and commonalities in the regulation of YPEL gene expressions, as well as structural similarities among YPEL proteins, render the deciphering of functional features of a YPEL protein in cellular processes in the presence of other YPELs difficult. We recently employed an inducible heterologous expression system, combined with dynamic proximity biotin labeling and mass spectrometry analyses, in non-tumorogenic COS7 cells, an immortalized African green monkey kidney fibroblast-like cell line that synthesizes endogenous YPEL protein(s). Results indicated that YPEL2 interacts with proteins involved in cellular processes, including stress response [30]. Based on these and our observations that YPEL2, as the endogenous YPEL protein(s), localizes to stress granules in response to oxidative stress, we suggested that YPEL2 participates in stress surveillance [30]. However, the mechanism(s) by which YPEL2 exerts its effects on cells remain unclear.

The basic mechanisms of cellular events, including proliferation, metabolism, and death, in the budding yeast *S. cerevisiae* share characteristics with those of evolutionarily distant species, such as humans, due to their highly conserved gene homology [31]. This allows the implementation of functional complementation approaches to address the features of homologous proteins. Since the yeast MOH1 (YBL049W) gene is the ortholog of the human YPEL gene family, we envisioned that complementing *MOH1* in a yeast model with a human YPEL gene could yield significant information about the role of a YPEL protein in cellular processes independently of other YPEL proteins.

A limited number of studies suggest that the MOH1 gene is a stationary phase-essential gene [32], as *MOH1*-deleted (*moh1Δ*) cells cannot survive under nutrient-depleted stationary phase conditions [32, 33]. This is consistent with observations that the exit from the stationary phase in response to a nutrient-rich environment augments a set of gene expressions, including *MOH1* [34]. Moreover, various stressors, including heat, zinc ion starvation, and hydrogen peroxide, modulate *MOH1* expression [35–38]. Extending these observations, *moh1Δ* cells have been reported to exhibit enhanced cell viability compared to the wild-type (WT) strain when treated with various stressors, including UV irradiation, chemicals, heat, and hyperosmotic shock [22]. Furthermore, the ectopic expression of *MOH1* or individual YPEL genes in the *moh1Δ* strain restores the WT phenotype in response to stressors [22]. In addition, recent studies reported that the genotoxic agent methyl methanesulfonate induces *MOH1* expression [39] and that *MOH1* may act as a stress response regulator, enhancing sensitivity to DNA damage in *Candida albicans* [40]. These studies collectively suggest that Moh1p, like the human YPEL2 protein, is involved in cell survival and stress response. However, how Moh1p exerts its effect on cellular phenotype is unclear. Since the elucidation of functional features of Moh1p could provide important clues about YPEL functions, here we used *S. cerevisiae* as a model system to initially explore the effects of *MOH1* on molecular events. Our findings, obtained using light and scanning electron microscopy (SEM), RNA sequencing (RNA-Seq), and Fourier Transform-Infrared Spectroscopy (FTIR), indicate that the deletion of *MOH1* in *S. cerevisiae* leads to constitutive molecular alterations that affect cell wall integrity, conferring selective advantages/sensitivities under specific stress conditions. Our results suggest that Moh1p constitutively influences metabolic and physiological processes critical for selective stress adaptation and cell survival.

RESULTS

Structural analysis of Moh1p and its similarity to YPEL proteins

Although the YPEL protein family is structurally conserved, most analyses have focused on primary sequence. Alignments based on the highly conserved cysteine residues reveal a striking amino acid identity among YPEL proteins, with numerous identical residues forming the Yippee domain. This domain, which contains two cysteine pairs separated by 52 amino acids (Cys-X_2-Cys-X_{52}-Cys-X_2-Cys), is predicted to form a zinc-binding pocket [1, 2] critical for folding and generating a presumably ligand-binding aromatic cage [41, 42].

To assess the relationship between yeast Moh1p and human YPEL proteins, we performed *in silico* analyses. Multiple sequence alignment (Clustal Omega, visualized with Jalview) [43, 44] confirmed that human YPEL1–4 share ~83% identity, while YPEL5 is less similar (43.8–49.5%) (**Figure 1A**) [1, 2]. *S. cerevisiae* Moh1p shares 37.8% identity with YPEL2 and 31.4–40.2% with other YPEL proteins. Secondary structure predictions using the JPred4 server [45] indicated that both Moh1p and YPEL2 are rich in β-strands (**Figure 1B**). Tertiary structure models using AlphaFold and visualization with

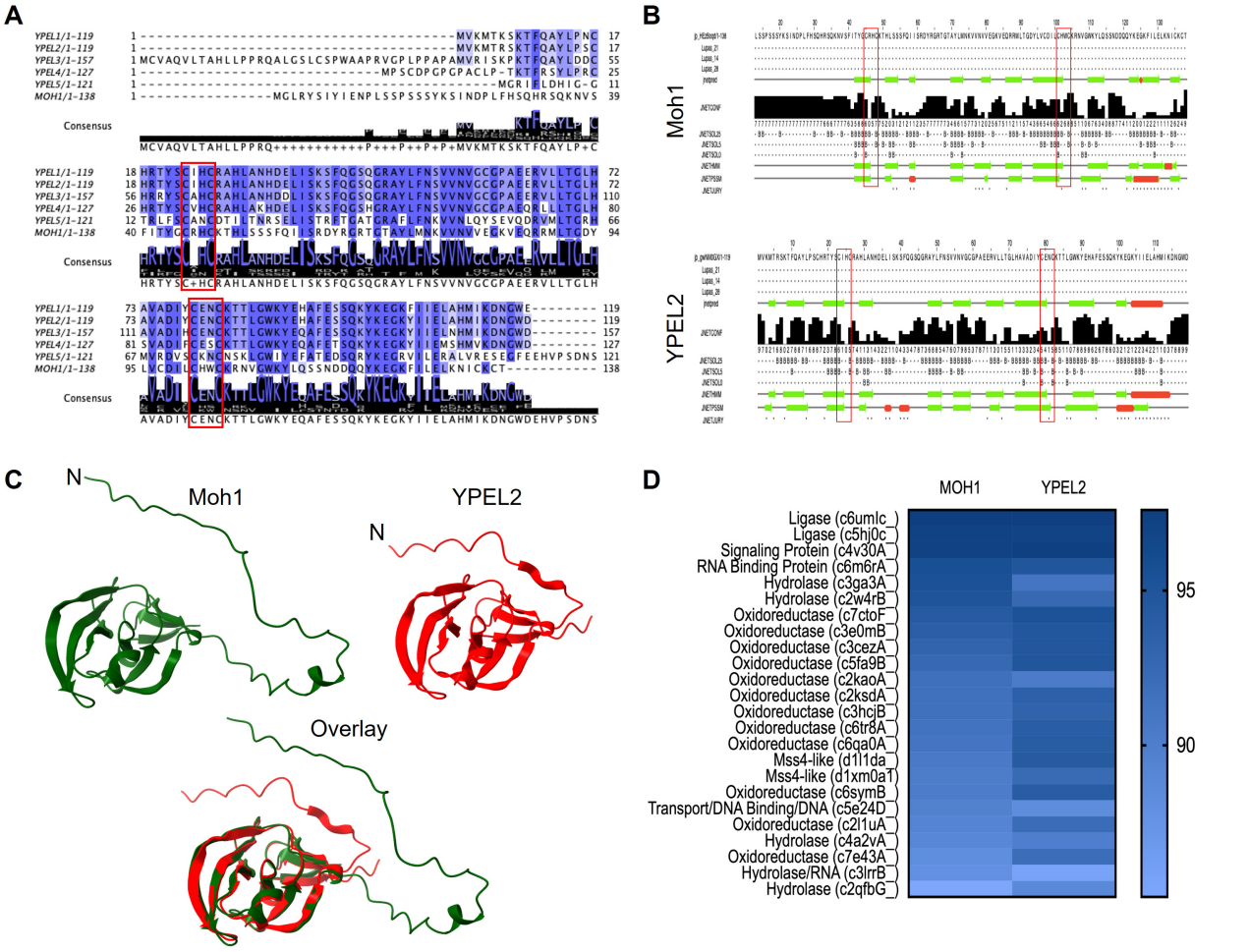

FIGURE 1 ● ***In silico* analyses of Moh1 and the YPEL family proteins**. **(A)** The alignment of the amino acid sequence of YPEL proteins and Moh1. Red squares indicate CXXC motifs. **(B)** Secondary structure analysis of Moh1 and YPEL2 with the jPred server **(C)**. Prediction and superimposition of tertiary structures of YPEL2 and Moh1 with the AlphaFold server using the ChimeraX molecular visualization program. **(D)** The Phyre2 web tool was used for the homology modeling of Moh1 and YPEL2.

ChimeraX [46–49] further showed that Moh1p and YPEL2 adopt similar globular, superimposable folds, differing mainly at their amino-termini (**Figure 1C**). Additional structural comparisons using Phyre2 [50] predicted high-confidence structural matches (>90%), suggesting that the Yippee domain is a conserved fold found across a broad range of functionally diverse protein families, including ligases, RNA-binding proteins, hydrolases, oxidoreductases, and Mss4-like proteins involved in essential cellular processes such as proteolysis, centromere priming, oxidative stress defense, and stress responses (**Figure 1D**, Supplementary Information Table S1) [51–59]. However, the functional role of the Yippee domain in these proteins remains largely unclear. Nonetheless, *MOH1* has been reported to be essential for survival in the stationary phase, as *moh1Δ* cells are unable to proliferate under nutrient-depleted, respiration-dependent conditions [32, 33, 60]. Consistent with this, the expression of *MOH1* was found to increase upon re-entry into growth from the stationary phase [34]. Additionally, *moh1Δ* cells exhibit altered viability under UV, heat, chemicals, and osmotic shock, which can be rescued by ectopic MOH1 or a YPEL gene expression [22]. These findings, together with our recent observations that YPEL2 is involved in oxidative stress surveillance [30], suggest a role for Moh1p in stress response.

Effects of *MOH1* deletion on cell survival under various stress conditions

Since *moh1Δ* cells cannot grow under nutrient-depleted, respiration-dependent conditions [33, 61], we aimed to validate this observation by comparing the colony-forming ability of WT and *moh1Δ* cells after 18 days in water, which mimics nutrient-depleted conditions (**Figure 2A**). We also included the *MOH1*-rescued strains in which *MOH1* (*moh1-i*) or a Flag-tagged *MOH1* (*f-moh1-i*) was reintroduced into the *moh1Δ* background to determine whether the insertion of *MOH1* rescues the phenotype observed in *moh1Δ* cells (**Figure 2A**). Consistent with earlier findings [32, 33], *moh1Δ* cells showed reduced survival compared to WT cells, while both rescued strains restored growth (**Figure 2A**). Importantly, the Flag tag did not impair Moh1p function, confirming that the *f-moh1-i* strain is suitable for protein-level analyses in our subsequent experiments.

Unlike the reduced ability of *moh1Δ* cells to resume growth after the stationary phase, *moh1Δ* cells were reported to grow comparatively better than WT cells following DNA damage, heat shock, and hyperosmotic shock treatments [22]. To further examine the growth and survival of yeast cells in response to

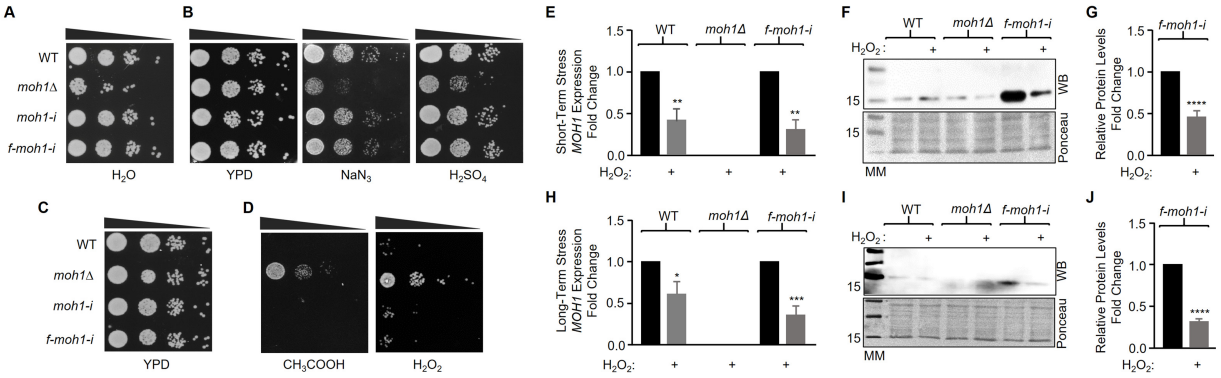

FIGURE 2 ● Spot tests of yeast strains grown on agar plates without or with a stressor. **(A)** A single colony from WT, *moh1Δ*, *moh1-i*, and *f-moh1-i* strains was grown in YPD overnight. 50 × 10^6 cells were subcultured into 20 mL of YPD at a ratio of 1:100 and grown for one week. Cells were then washed twice with 1 M Sorbitol and once with sterile distilled water, and resuspended in 20 mL of sterile distilled water. Cells were incubated at 30°C with shaking at 180 rpm. Cultures were collected for a spot test at day 14 and spotted on agar plates with 10-fold serial dilutions (Black triangles). Cells were incubated at 30°C for 40 hours and photographed. **(B–D)** Cells from subcultures were grown until OD_{600} 0.4–0.6. Cells, 2.5 × 10^6 cells/mL, were spotted with 10-fold serial dilutions on **(B)** YPD-Agar plates containing none (YPD) or 0.4 mM NaN3, or 0.22% H_2SO_4, **(C)** none (YPD), **(D)** 40 mM CH_3COOH, or 3.25 mM H_2O_2. Plates were incubated at 30°C for 40 hours and photographed. **(E–J)** Expression by RT-qPCR **(E & H)** and synthesis by WB using the Flag antibody **(F & I)** of *MOH1* in WT, *moh1Δ*, and *f-moh1-i* cells after exposure to short-term, 45 min **(F & G)** or long-term stress, 40 h. **(I & J)** Expression of *MOH1* using primers specific to *MOH1* was normalized to transcript levels of *YPR062W* (*FCY1*) and *YNL219C* (*ALG9*) as internal controls in RT-qPCR. In WB analysis, the level of Flag-Moh1 migrating at ~16 kDa in the absence of H_2O_2 was set to one and compared to that observed in the presence of H_2O_2. A band of similar molecular mass was also detected in both WT and *moh1Δ* strains, indicating that it represents a non-specific signal. Ponceau staining was used as a control for equal protein loading. Molecular weight markers are indicated in kDa. A Student's t-test was conducted for statistical analyses. *, **, ***, and **** indicate $p < 0.05$, $p < 0.01$, $p < 0.001$, and $p < 0.0001$, respectively.

various stress conditions, we subjected the WT and *moh1Δ* strains to 0.4 mM sodium azide (NaN_3, a cytochrome oxidase blocker for the mitochondrial respiratory chain), 40 mM acetic acid (CH_3COOH, a weak organic acid), 0.22% sulfuric acid (H_2SO_4, a strong acid), and 3.25 mM hydrogen peroxide (H_2O_2, an oxidative stress inducer) [62–66]. Briefly, strains cultured in YPD medium to the logarithmic phase were spotted on YPD agar plates containing each stressor. Stressor concentrations were chosen empirically to produce measurable but non-lethal effects (Supplementary Information Fig. S1). Spot assays showed that in the presence of NaN_3 or H_2SO_4, WT cells showed better survival compared to *moh1Δ* cells (**Figure 2B**). In contrast, the *moh1Δ* cells were more resistant to H_2O_2 and CH_3COOH (**Figure 2D**). Similarly, introduction of *YPEL2* into *moh1Δ* cells restored stress phenotypes, consistent with functional conservation between Moh1p and YPEL2 (Supplementary Information Fig. S2). Furthermore, spot assays with YPRG, glycerol, low-glucose conditions at different temperature and different media pH revealed no significant growth differences between the strains (Supplementary Information Fig. S3), indicating that *MOH1* deletion does not broadly impair metabolic flexibility or pH tolerance.

Taken together, these findings suggest that the role of *MOH1* in stress survival is dependent on the type of stress encountered. While the presence of Moh1p promotes cell survival and growth under respiratory and sulfuric acid stress, the enhanced tolerance of *moh1Δ* cells to oxidative and acetic acid stress points to a potential repressive function of Moh1p under these conditions.

Environmental stresses differentially modulate Moh1p levels

Since the expression of *MOH1* increases during re-entry into growth from the stationary phase [32], consistent with its role in the exit from the stationary phase and recovery from nutrient depletion [33], we wanted to determine whether other stressors modulate *MOH1* expression. We monitored transcript and/or protein levels under oxidative and acidic stress. We first analyzed the changes in levels of *MOH1* transcript upon short-term (45 min) (**Figure 2E**) and long-term (40 h) (**Figure 2G**) stress. RT-qPCR revealed that short-term and long-term exposure to H_2O_2 repressed *MOH1* mRNA levels in WT and *f-moh1-i* cells (**Figure 2E** and **2G**). On the other hand, short-term and long-term exposure to H_2SO_4 resulted in elevated *MOH1* mRNA levels in WT and f-moh1-i cells (Supplementary Information Fig. S4A and S4D). We next examined the changes in f-Moh1 protein levels with WB using the anti-Flag antibody. In Western blot (WB) analyses, for which we used Ponceau staining as the equal loading control, the Flag antibody detected a non-specific protein species that shows an electrophoretic migration similar to f-Moh1 (approximately 17 kDa). Nevertheless, consistent with the change in levels of the *MOH1* or *f-moh1* transcript, f-Moh1 protein levels were effectively decreased after both short-term and long-term H_2O_2 treatment (**Figure 2F–2J**). In contrast, short-term or long-term treatment of yeast cells with H_2SO_4 augmented f-Moh1 protein levels (Supplementary Information Fig. S4B, S4C, S4E, and S4F). Given that *moh1Δ* cells are hypersensitive to H_2SO_4 (**Figure 2B**), this increase is consistent with a protective role for Moh1p under strong acid stress.

These observations suggest that Moh1p levels are dynamically regulated in response to stress, with distinct stress conditions exerting differential effects on its abundance. Specifically, oxidative stress suppresses *MOH1* expression and Moh1p synthesis, whereas acid stress induces them, indicating a tuning mechanism that enables cells to adjust Moh1p levels to promote survival under diverse environmental challenges.

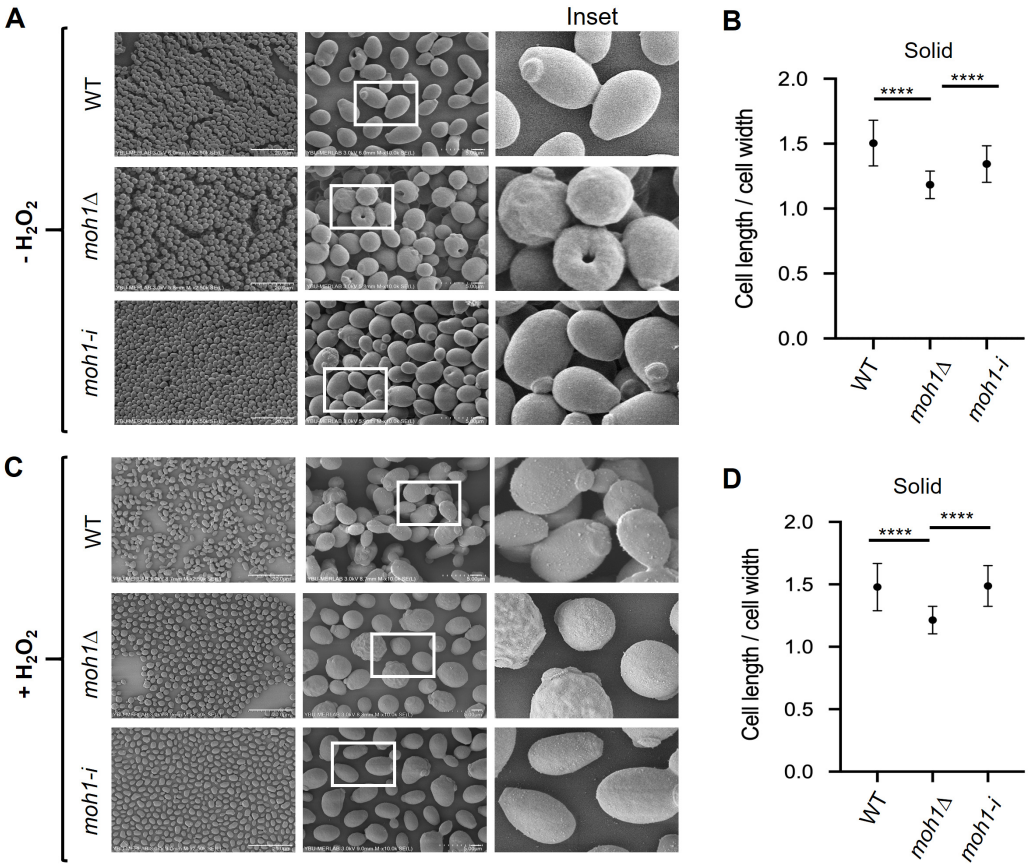

FIGURE 3 ● **SEM of yeast strains grown on solid media in the absence or presence of H_2O_2 as a stressor. (A and C)** WT, *moh1Δ*, and *moh1-i* cells were grown on YPD-Agar plates containing none (-) or 3.25 mM H_2O_2 for 40 hours at 30 °C. Colonies were removed and transferred into vials containing 4% glutaraldehyde in water for fixation, followed by dehydration with ethanol and air drying. Samples were coated with gold and imaged using a Scanning Electron Microscope (SEM). White squares indicate the Inset. Scale bars are shown. **(B and D)**. The cell length and width ratio of yeast strains in the absence **(B)** or the presence **(D)** of H_2O_2 was graphed using 50 cells from images. A Student's t-test was conducted for statistical analyses. **** indicates significant difference ($p < 0.0001$).

MOH1 deletion alters cell shape and surface topology

moh1Δ cells exhibited a pronounced tendency to form clumps compared to WT cells when viewed with light microscopy (Supplementary Information Fig. S5). To further examine cellular morphology, we employed scanning electron microscopy (SEM), a technique widely used to investigate the surface ultrastructure of biological specimens [67, 68], to analyze the surface structure of WT, *moh1Δ*, and *moh1-i* strains grown on agar plates (**Figure 3**) and in liquid culture (Supplementary Information Fig. S6). To assess potential growth stage-dependent differences, both logarithmic-phase (Supplementary Information Fig. S6A-D) and stationary-phase (Supplementary Information Fig. S6E-H) cultures were examined. Additionally, to determine whether oxidative stress influences morphological features, the strains were also cultured in the presence of H_2O_2.

Cell morphology was evaluated based on the length-to-width ratio. Under all tested conditions, WT and *moh1-i* cells retained their characteristic ovoid shape, with an average ratio of ~1.5. In contrast, *moh1Δ* cells appeared significantly more spherical, with ratios approaching 1 (**Figure 3** and Supplementary Information Fig. S6). The morphological differences between *moh1Δ* and the control strains were even more evident in surface topography. While WT and *moh1-i* cells displayed smooth surfaces under all growth conditions or H_2O_2 exposure, *moh1Δ* cells showed roughened surfaces with prominent protrusions and indentations (**Figure 3** and Supplementary Information Fig. S6).

These findings demonstrate that deletion of *MOH1* results in constitutive morphological abnormalities, characterized by rounder cells with irregular surface structures and a tendency to clump, irrespective of growth phase or oxidative stress. This points to a critical role of Moh1p in maintenance of cellular architecture, while also implicating it in stress response and/or adaptive processes.

Effects of *MOH1* deletion on the transcriptomic profile of *S. cerevisiae*

To gain insight into the molecular mechanisms that underly the effects of *MOH1* deletion, we compared the transcriptomic profiles of the WT and *moh1Δ* strains by high-throughput RNA sequencing (RNA-Seq) of cells from spot tests. Differentially expressed genes (DEGs) were identified using the DESeq2 package in R. Genes were considered differentially expressed if they exhibited a $\log_2$ fold change ≤ -0.6 or $\geq +0.6$ and an adjusted p-value below 0.05.

We identified 52 DEGs in the *moh1Δ* strain relative to WT, including *MOH1* as expected (**Figure 4A**, Supplementary

Information Table S2). Of these, while 39 genes were upregulated, 13 genes were downregulated. According to Saccharomyces Genome Database (SGD; https://www.yeastgenome.org/), all DEGs are stress-responsive (Supplementary Information Table S2) except the long non-coding RNA *YNCJ0028C* (*IRT1*), and the 5S ribosomal RNA *YNCL0018W* (*RDN5-1*). Using RT-qPCR, we verified the differential expression of *YMR169C* (*ALD3*), *YPL223C* (*GRE1*), and *YOR247W* (*SRL1*) (Supplementary Information Fig. S7). These genes were selected due to their association with stress responses and cell wall integrity [34, 69–71].

To explore the functional implications of these DEGs, we analyzed gene ontology (GO) terms for biological functions, using SGD, Metascape ([72], https://metascape.org/), and STRING ([73], https://string-db.org/) databases (**Figure 4**, Supplementary Information Table S3 and Fig. S8). Five DEGs corresponded to dubious ORFs (*YDR048C, YMR324C, YGL177W*, and *YHR214W-A, YCR018C-A*), while four DEGs (*YKL068W-A, YBL048W,* and *YJR115W)* encode proteins of unknown functions. The Metascape analysis of the remaining DEGs indicates enrichments in the GO-terms of metabolic pathways, glycolysis, as well as biogenic amine, hexose, sulfur compound metabolic, and mRNA catabolic processes (**Figure 4B-C**). Together with SGD Database and STRING Database results, these findings suggest that *MOH1* is involved in networks critical for balancing carbon, nitrogen, and sulfur metabolism, thereby supporting cellular physiology and morphology.

Because pathway-level enrichments were based on a relatively limited number of DEGs (44 genes with known or predicted functions), we performed manual annotation of individual genes. Among the upregulated DEGs, *YJR155W* (*AAD10*), *YMR169C* (*ALD3*), *YGR155W* (*CYS4*), *YLR299W* (*ECM38*), *YPL281C* (*ERR2*), *YMR323W* (*ERR3*), *YER091C* (*MET6*), *YGR087C* (*PDC6*), *YOL136C* (*PFK27*), *YAL023C* (*PMT2*), *YMR322C* (*SNO4*), *YJR159W* (*SOR1*), *YDR297W* (*SUR2*), *YGR144W* (*THI4*), and *YBR242W* (*YB92)*, for example, encode enzymes involved in key metabolic processes including nucleic acid, protein, lipid, and carbohydrate metabolism, suggesting that Moh1p plays a central role in metabolic regulation. Additionally, *YGL158W* (*RCK1*), which encodes a threonine protein kinase that reduces ROS levels and promotes oxidative stress tolerance [74], was also upregulated, potentially contributing to the enhanced oxidative stress resistance of *moh1Δ* cells.

Conversely, several genes critical for cytoskeletal organization, cytokinesis, vesicular trafficking, membrane integrity, and cell wall stability, including *YGL263W* (*COS12), YMR032W* (*HOF1*), *YLR190W* (*MMR1*), *YAL023C* (*PMT2*), and *YOR247W* (*SRL1*), were downregulated. Furthermore, *YOR315W* (*SFG1*), a transcription repressor of genes involved in cell wall degradation [75, 76], was also downregulated in *moh1Δ* cells. Deregulated expression of these genes may account for the morphological alterations observed in *moh1Δ* cells.

Collectively, these findings position Moh1p as a key regulator of metabolic adaptation and cellular architecture.

MOH1 deletion alters the biomolecular composition of *S. cerevisiae*

Changes in cellular morphology and expression of genes related to lipid, protein, and carbohydrate metabolism suggest that the macromolecular composition and organization in *moh1Δ* cells are altered. To assess these biochemical changes, we employed FTIR, which provides a comprehensive biochemical fingerprint of cells by capturing unique vibrational spectra of proteins, lipids, and polysaccharides [77–85]. FTIR enables both quantitative and qualitative assessment of macromolecular composition and organization [77–85] and has been widely applied to monitor biochemical changes in yeast under various conditions, including stress and apoptosis [86–94].

Given the high dimensionality of IR spectral data, we applied principal component analysis (PCA) to reduce data complexity and visualize strain-specific spectral differences [95–99]. The PCA results demonstrated a clear separation between WT and *moh1Δ* cells, explaining 89% of the total variance (PC1: 82%, PC2: 7%), which reflects substantial compositional divergence between the two strains (**Figure 5A**). Hierarchical clustering analysis (HCA) [100] further supported these findings by revealing distinct clustering patterns for WT and *moh1Δ* strains (**Figure 5B**). The corresponding IR band assignments for the spectral features are provided in Supplementary Information Table S4.

Quantitative comparisons of spectral bands of lipid regions indicate significant reductions in saturated fatty acids and an increase in bandwidth values of the CH_2 asymmetric stretching band, along with increased lipid/protein ratio in *moh1Δ* cells (**Figure 5C-E**). These changes point to altered lipid levels, modified composition and packing, and reorganization of membrane structures, processes critical for cellular stress adaptation and response [101–103]. FTIR analysis also revealed a change in protein secondary structures, indicated by increases in the amide I and amide II band intensities, as well as an altered protein environment reflected in a decrease in the Amide I/Amide I + Amide II ratio (**Figure 5F-H**) [104–106]. Moreover, elevated protein carbonylation and an increased carbonyl/lipid ratio indicate enhanced oxidative damage to both proteins and lipids (**Figure 5I-J**) [107, 108]. Notably, *moh1Δ* cells displayed elevated levels of polysaccharides, including β-(1,3)-glucan, β-(1,6)-glucan, and mannan (**Figure 5K-M**), features that are hallmarks of a remodeled cell wall [109, 110].

Together, these findings demonstrate that *MOH1* deletion leads to widespread biochemical and structural changes, including alterations in lipid and protein profiles, oxidative damage response, membrane reorganization, and cell wall remodeling, that likely underlie the selective stress adaptations observed in *moh1Δ* cells.

MOH1 deletion reduces intracellular ROS by limiting H_2O_2 uptake

Increased resistance to H_2O_2 in *moh1Δ* cells suggests that Moh1p is directly involved in mitochondrial ROS production and/or clearance, or indirectly through cell wall remodeling,

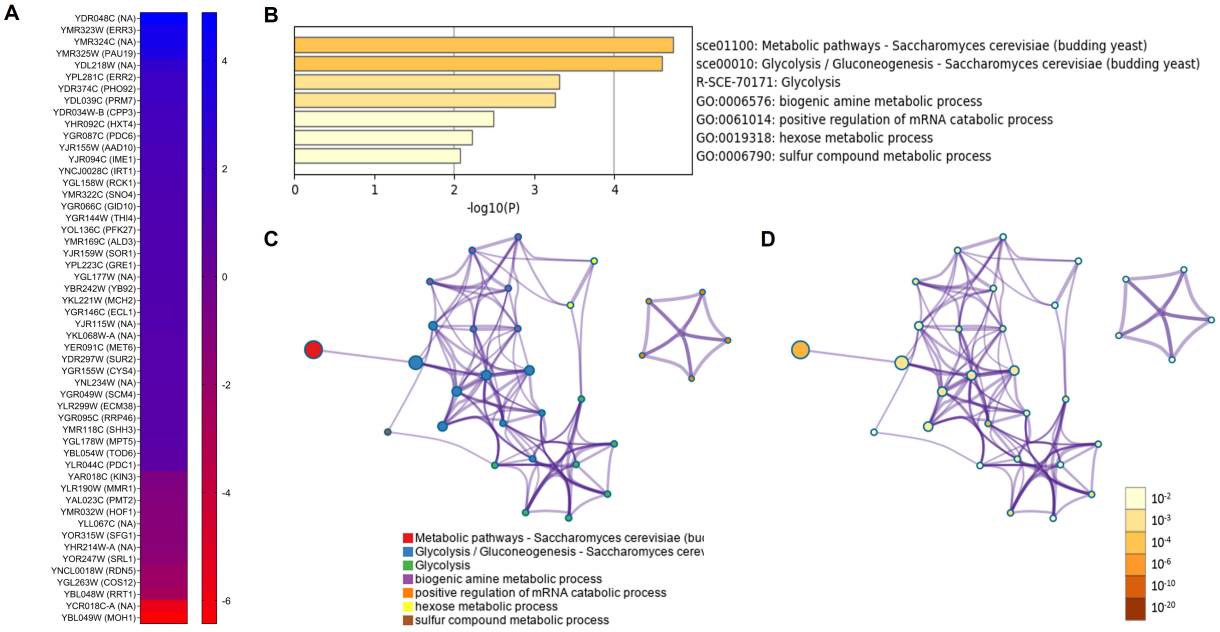

FIGURE 4 ● **Identification of differentially expressed genes as a result of *MOH1* deletion by RNA-Seq.** Total RNA of WT and *moh1Δ* cells from spot tests on YPD plates was subjected to high-throughput RNA sequencing. RNA-Seq results were analyzed using the DESeq2 package in R, and genes were considered differentially expressed if they exhibited a $\log_2$ fold change ≤−0.6 or ≥+0.6 and an adjusted p-value below 0.05. **(A)** Heatmap of DEGs, **(B–D)** Metascape results of DEGs are presented as **(B)** Enriched terms, **(C)** Network of enriched term nodes, and **(D)** Enriched term nodes colored by p-value.

which is critical for reducing/blocking H_2O_2 penetration/uptake into the cell. Previous studies indicated that H_2O_2 produced intracellularly or provided exogenously activates cellular responses that enhance resistance to oxidative stress by upregulating antioxidant enzymes, including catalase [111], which catalyzes the decomposition of H_2O_2 to water and oxygen [112]. However, at elevated levels, H_2O_2 represses catalase activity, resulting in cell death [113].

Indeed, H_2O_2 treatment under short-term stress (45 min) at low concentration (0.325 mM) activated catalase activity in WT and *moh1Δ* strains but represses it at high concentration (3.25 mM), as we have used throughout this study, to those levels observed without treatment (**Figure 6A**). Under the high H_2O_2 concentration used here, the suppression of catalase activity, thereby minimization of differences in detoxification, in both strains provided an opportunity to assess whether the remodeled cell wall reduces/blocks H_2O_2 uptake/penetration into the cell. To examine this issue, we monitored relative ROS levels in WT and *moh1Δ* cells, with or without short-term H_2O_2 treatment (**Figure 6B-C** and **6E**). As a reporter for ROS levels, we used 2′-7′-Dichlorodihydrofluorescein diacetate (H_2DCFDA), which, upon oxidation, is converted into a fluorescent dye (2′,7′-dichlorofluorescein) and can be detected quantitatively by flow cytometry [114]. To specifically assess mitochondrial ROS contribution, we included antimycin A (AMA), a well-established inducer of mitochondrial ROS by inhibiting complex III of the electron transport system [115], as a positive control. Under AMA treatment, both WT and *moh1Δ* cells exhibited comparable ROS levels, indicating that mitochondrial ROS generation is not significantly altered in the absence of *MOH1* (**Figure 6D**). On the other hand, in the absence of H_2O_2, *moh1Δ* cells exhibited lower basal ROS levels compared to WT cells (**Figure 6B** and **6E**), suggesting a role for Moh1p in basal ROS generation. Upon exposure to H_2O_2, ROS levels increased substantially in WT cells but remained largely unchanged in *moh1Δ* cells (**Figure 6C** and **6E**). In contrast, treatment with AMA induced comparable increases in ROS levels in both strains (**Figure 6D**). These results indicate that the reduced ROS accumulation observed in *moh1Δ* cells under H_2O_2 treatment is not due to impaired mitochondrial ROS production but rather reflect reduced cellular uptake of H_2O_2. Together with FTIR and SEM data, these findings suggest that the remodeled cell wall of *moh1Δ* cells may limit H_2O_2 permeability/uptake, thereby conferring resistance to oxidative stress induced with H_2O_2.

To further assess whether altered cell envelope properties contribute to the reduced intracellular ROS accumulation observed in *moh1Δ* cells, we examined their sensitivity to cell wall- and membrane-perturbing agents. In spot assays (**Figure 6F** and **6G**; Supplementary Information, Fig. S11), *moh1Δ* cells exhibited increased resistance to Congo red, a dye that binds β-glucan and interferes with cell wall assembly [116–118], but increased sensitivity to Sodium Dodecyl Sulfate (SDS), a detergent that disrupts plasma membrane integrity [119, 120]. The resistance to Congo red, despite increased β-glucan levels as indicated by FTIR, suggests reduced accessibility of cell wall polysaccharides, likely due to altered wall organization and mannan masking a results of increased mannan concentrations [116, 117] as also observed with our FTIR analysis. In contrast, the heightened sensitivity to SDS indicates compromised membrane integrity or defective coordination between the cell wall and plasma membrane. These findings are consistent with our FTIR and SEM results and suggest that *MOH1* deletion leads to cell envelope remodeling that likely alters cell permeability to H_2O_2.

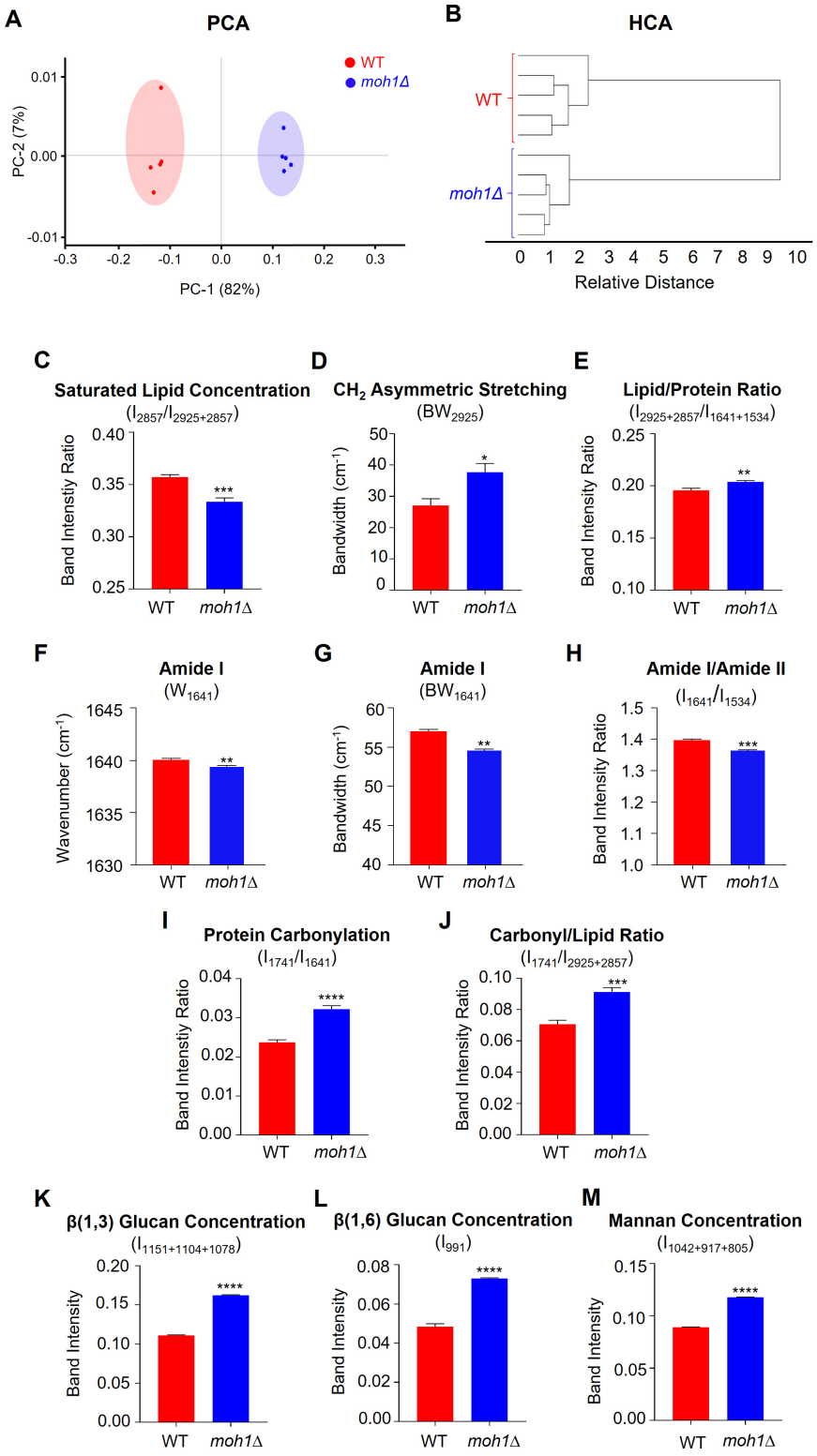

FIGURE 5 ● **Comparative analyses of WT and *moh1Δ* cells with FTIR**. (**A**-**M**) WT or *moh1Δ* cells spotted on the YPD-Agar plates were incubated at 30°C for 40 hours. Cells were scraped from the agar plate into sterile distilled water and centrifuged at 1000 rpm for 5 minutes to form a pellet. After washing with distilled water, 2×10^8 cells were concentrated, placed on an ATR crystal, and dried with N_2 for 5 min. Five biological replicates of WT and *moh1Δ* cells were subjected to FTIR analyses as two technical repeats. (**A**) PCA score, (**B**) HCA dendrogram. FTIR results of the WT and *moh1Δ* strains (**C**-**M**) were quantified as band intensity ratios, band width or band intensity for (**C**) saturated lipid concentrations, (**D**) CH_2 asymmetric stretching, (**E**) lipid/protein ratio, (**F**) amide I (**G**) amide I, (**H**) amide I/amide II, (**I**) protein carbonylation, (**J**) carbonyl/lipid ratios, (**K**) β-(1,3)-glucan concentration, (**L**) β-(1,6)-glucan concentration, and (**M**) mannan concentration. The results were presented as the mean ± S.E.M. with a student's t-test for the statistical significance of the quantitative spectral results with * $p < 0.05$, ** $p < 0.01$,**** $p < 0.0001$.

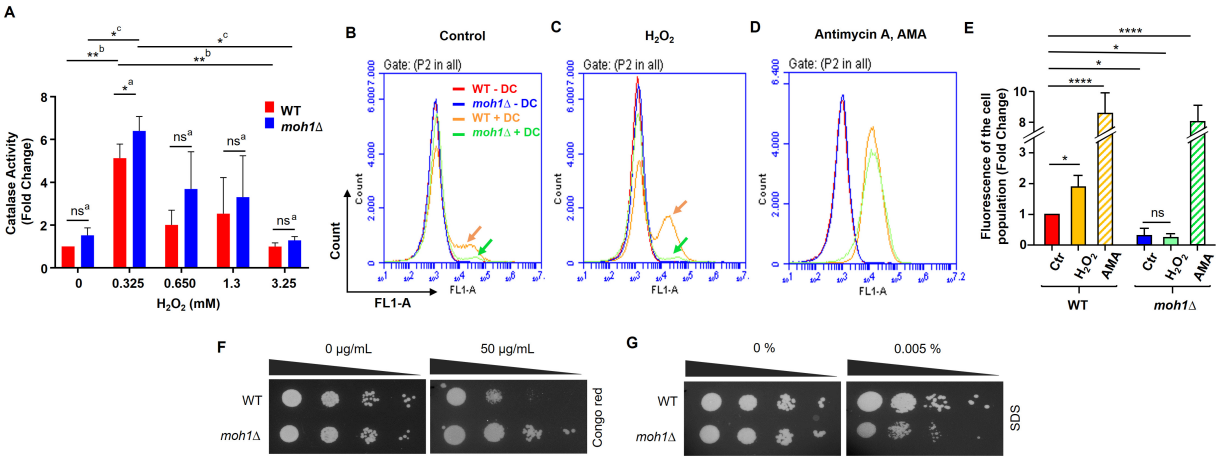

FIGURE 6 ● The effects of H_2O_2 on intracellular ROS levels. (A) WT and *moh1Δ* strains grown in YPD with an OD_{600} of 0.4–0.6 were treated without (0), or with 0.325, 0.650, 1.3, or 3.25 mM H_2O_2. Cells were then processed for and subjected to a catalase activity assay. The graph presented as mean ± S.E.M. of three independent determinations indicates fold changes in catalase activity of WT cells in the absence of H_2O_2 (0), which was set to one. Statistical significance of the results was determined using Student's t-test (∗p < 0.05, and ∗∗p < 0.01); ns denotes non-significant. [a] indicates significant change compared to WT at indicated concentrations of H_2O_2; [b] denotes responses observed with WT cells changes at 0.325 and 3.25 mM H_2O_2; and [c] indicates significant changes responses observed with the moh1Δ strain at 0.325 and 3.25 mM H_2O_2. **(B–E)** WT and *moh1Δ* cells grown in YPD with an OD_{600} of 0.4–0.6 were treated without (control), or with 3.25 mM H_2O_2, or 25 µg/mL Antimycin A (AMA) for 45 minutes. Cells were treated without or with 20 µM reactive oxygen species indicator H_2DCFDA (DC) for 45 minutes at 30°C. Cells were then washed twice with PBS by centrifugation at 6000 × g for 3 minutes. **(B-D)** Fluorescence intensity was measured with a flow cytometer by using the FL1-A channel with excitation at 488 nm and emission at 525 nm. A minimum of 100,000 events was recorded per sample. Representative images from the same experiment, conducted as three biological replicates, are shown. **(E)** The graph indicates fold changes in fluorescence of the cell population normalized to the WT control, which was set to one. Results are presented as mean ± S.E.M. of three independent determinations, and statistical significance of the quantitative spectral results was determined using Student's t-test (∗p < 0.05, ∗∗p < 0.01, and ∗∗∗∗p < 0.001); ns denotes non-significant. **(F)** WT and *moh1Δ* cells spotted on YPD-Agar plates containing 0 or 50 µg/mL Congo red, or **(G)** 0% or 0.005% SDS with 10-fold serial dilutions (Black triangles). Cells were incubated at 30 °C for 40 hours and photographed.

DISCUSSION

We present evidence that deletion of *MOH1* triggers coordinated molecular changes that reshape the physiology and cellular architecture of *S. cerevisiae*. Phenotypic assays reveal stress-specific survival responses in the *moh1Δ* strain. Integrated RNA-Seq and FTIR analyses demonstrate that deletion of *MOH1* results in transcriptional reprogramming and metabolic remodeling, reflected in altered lipid, protein, and cell wall polysaccharide composition and are consistent morphological changes observed by SEM independently of stress. Functional assays further show that increased resistance of *moh1Δ* cells to H_2O_2 is not due to enhanced ROS detoxification but rather to reduced intracellular ROS accumulation. Together with Congo red resistance and SDS sensitivity, these results indicate altered cell envelope organization and decreased permeability to exogenous H_2O_2. We therefore propose that Moh1p links gene expression and metabolism to cell envelope structure, thereby modulating cell envelope permeability and conferring selective stress resistance.

Our findings identify *MOH1* as a key regulator of cell envelope homeostasis, linking metabolic state, gene expression, and structural organization to stress adaptation in *S. cerevisiae*. RNA-Seq analysis revealed coordinated transcriptional changes in *moh1Δ* cells affecting metabolism, redox balance, and cellular architecture. Although relatively few genes were differentially expressed, their functional clustering provides important mechanistic insight. Upregulation of glycolytic and sugar metabolism genes, including *PFK27, PDC6, SOR1, ERR2, and ERR3*, suggests metabolic reprogramming to sustain energy production and biosynthetic demands associated with cell envelope remodeling [121]. Consistent with this, our FTIR analyses indicated alterations in lipid and carbohydrate composition, supporting a role for Moh1p in maintaining the metabolic balance required for proper envelope organization. This is accompanied by enrichment of sulfur metabolism genes including *MET6* and *CYS4*, likely reflecting increased glutathione-associated redox buffering capacity and compensatory maintenance of cellular homeostasis. In addition, upregulation of oxidative stress-related *ALD3*, *GRE1*, and *RCK1* expressions, is consistent with activation of environmental stress response pathways [121–123]. While these transcriptional changes may contribute to improved oxidative stress tolerance, they are not sufficient to explain the observed H_2O_2 resistance. Instead, functional assays demonstrate that reduced intracellular ROS accumulation in *moh1Δ* cells is primarily due to decreased uptake of exogenous H_2O_2 rather than altered mitochondrial ROS production. This is supported by comparable ROS responses in WT and *moh1Δ* cells following antimycin A treatment, indicating that mitochondrial ROS generation remains intact. Under the high H_2O_2 conditions used in this study, catalase activity is suppressed in both strains, further supporting permeability rather than detoxification as critical contributor of intracellular ROS levels.

Consistent with this, *moh1Δ* cells display resistance to Congo red but sensitivity to SDS. Resistance to Congo red suggests reduced accessibility of *β*-glucan due to increased mannan masking and altered wall organization, while SDS sensitivity indicates compromised plasma membrane integrity or defective coordination between the membrane and cell wall. Together, these findings suggest that *MOH1* is required

for proper cell envelope organization and permeability control. Indeed, transcriptional downregulation of *HOF1*, *SRL1*, *COS12*, and *PMT2* involved in cytokinesis, vesicular trafficking, and cell wall integrity, and of SFG1 further support deregulated cell wall remodeling. *moh1Δ* cells exhibit stress-specific phenotypes, including increased resistance to CH_3COOH and heightened sensitivity to NaN_3 and H_2SO_4. CH_3COOH induces cytoplasmic acidification and oxidative stress, whereas NaN_3 inhibits mitochondrial respiration and H_2SO_4 causes strong acid and membrane stress [124, 125]. These differential responses suggest reprogramming of stress adaptation pathways, resulting in functionally altered envelope remodeling and selective resistance to stressors. Future studies combining Moh1p with membrane structural mutants will be important for further elucidating the mechanistic role of Moh1p in cellular envelope regulation and responses to environmental stress.

Although it is evident that Moh1p plays a role in the physiology and structural organization of *S. cerevisiae*, the mechanisms by which it functions remain unclear. Our *in silico* analyses indicate that Moh1p, like other members of the YPEL protein family, contains a single structural domain: the Yippee domain (**Figure 1**). Homology modeling, aimed at predicting the Moh1p function through the Yippee domain, reveals structural similarities with Yippee-like domains, MeDIY [54] or the CULT/*β*-tent fold [41], of proteins from both prokaryotes and eukaryotes, and are associated with oxidoreductase, RNA binding/hydrolysis, and chaperone activities, suggesting an evolutionary link [1, 2, 41, 54]. One of the key challenges in understanding the biological function of Yippee domains is the identification of endogenous ligand(s) [41]. While the Yippee domain is structurally conserved, differences in amino acid composition across various proteins may result in distinct protein interaction profiles and specialized binding surfaces, leading to selective ligand recognition. MSRA and MSRB oxidoreductase enzymes, for example, reduce methionine sulfoxide to generate unmodified methionine, thereby contributing to antioxidant defense [58, 126, 127]. Despite the Yippee domain, it is unlikely that Moh1p, like other YPEL proteins [30], is a methionine-sulfoxide reductase, as it lacks the invariably conserved cysteine-containing motifs essential for the catalytic activity of MSRA (GCPWG) or the MSRB (RXCXN) [58]. On the other hand, the MeDIY domain of Mis18 proteins is shown to be a critical interacting surface for dimerization/oligomerization of the proteins, as well as CENP-A loading at the centromere for chromosome segregation [54, 128]. It is therefore possible that the interaction of Moh1p with various proteins, dependent upon the metabolic state of the cell, triggers sets of events critical for the physiology and structural organization of *S. cerevisiae*.

Proteins function within dynamic networks of interacting partners whose composition changes in response to cellular and environmental cues [129, 130]. Although we were unable to acertain the intracellular localization of Moh1p, likely due to misfolding of fluorescently tagged constructs, Moh1p was reported to interact with some members of primarily cytoplasmically localized molecular chaperone CCT/TRiC (Chaperonin Containing TCP-1/T-complex protein Ring Complex) and GID (Glucose-Induced Degradation complex) complexes using immuno-affinity purification coupled with mass spectrometry [131]. The CCT/TRiC complex is a cytosolic type II chaperonin composed of two stacked rings, each containing eight distinct subunits (CCT1-CCT8), which mediate ATP-dependent folding of newly synthesized and stress-denatured proteins [132, 133]. Through conformational changes driven by ATP binding and hydrolysis, CCT facilitates folding of key substrates involved in cytoskeletal organization, signaling, and cell cycle regulation, including actin and tubulin [132–134]. Although, to our knowledge, no functional studies have established Moh1p as a regulator of these complexes, interaction of Moh1p with with CCT2 and CCT3 subunit proteins [131] suggests a potential role in modulating chaperone-mediated protein folding.

The conserved GID and GID (Glucose-Induced Degradation complex) complex is a multi-subunit E3 ubiquitin ligase composed of core Gid1, Gid2, Gid5, Gid7, Gid8, and Gid9 [135] along with Gid4 [135], Gid10 [136], and Gid11 [137, 138] subunits that function in a condition-specific manner. The GID complex regulates proteasomal degradation of metabolic enzymes, particularly during transitions between gluconeogenesis and glycolysis [135–139]. Upon glucose reintroduction, activation of the complex through the incorporation of substrate receptors like Gid4 enables the ubiquitination and degradation of enzymes such as Fbp1, Pck1, Mdh2, and Icl1 [140, 141]. Moh1p was reported to interact with the multiple core GID subunits by immuno-affinity purification coupled with mass spectrometry [131]. We observed *GID10* expression is elevated in the *moh1Δ* strain (**Figure 4A** and Supplementary Information Table S2). Gid10, a stress-induced substrate receptor, shares substrate specificity with Gid4 [128], but also targets distinct proteins such as Art2, involved in plasma membrane quality control [142, 143]. These findings imply an altered GID-dependent proteolysis in *moh1Δ* cells under stress, linking GID activity to cellular envelope regulation [142, 143].

The interaction of Moh1p with the CCT/TRiC and GID complexes suggests a regulatory role in coordinating selective protein folding and degradation during environmental adaptation. This aligns with RNA-Seq data showing a metabolic shift toward glycolysis in *moh1Δ* cells, accompanied by changes in lipid, protein, and polysaccharide composition and corresponding cell wall alterations observed by SEM. These findings suggest that *moh1Δ* cells may reconfigure stress defenses through altered CCT and GID activity. The involvement of Moh1p in cellular response to various stressors could entail distinct integrated mechanisms ranging from transcription to post-translational processes, with proteostasis at their core. While detailed mechanistic analyses of each stress response would require targeted biochemical and genetic approaches, Moh1p may function as an adaptor linking CCT-mediated folding and GID-mediated degradation, thereby influencing cell fate under stress. Stress-dependent changes in Moh1p levels, as we observed in response to H_2O_2, or increases induced by H_2SO_4, could modulate its interactions with these complexes, leading to a functional state in the complexes permissive or inhibitory for selective protein folding

and degradation. Additionally, Moh1p may act as a sensor for monitoring pH changes or ROS levels that potentially trigger conformational alterations, influencing association with or dissociation from the CCT/GID complexes. Moh1p was also reported to be phosphorylated at two serine residues of the immediate amino-terminus region of the protein [144]. Such modifications could alter proteostasis and drive metabolic reprogramming by sterically or electrostatically hindering the interaction of Moh1p with the CCT/GID complexes. Further studies aimed at identifying ligands, direct binding partners, and spatial-temporal dynamics of Moh1p across stress gradients will be crucial in elucidating its mechanistic role within the proteostasis network of *S. cerevisiae*.

In summary, our results indicate that deletion of *MOH1* causes coordinated transcriptional, biochemical, and structural changes, including pronounced alterations in cell envelope properties and permeability to stressors. Together, these findings identify Moh1p as a critical link between intracellular metabolic processes and the cell surface, enabling selective resistance to environmental stress.

MATERIAL AND METHODS

Homology modeling

The alignment of amino acid sequences was carried out using Jalview [43] program (https://www.jalview.org/) with the ClustalOmega [44] plug-in (https://www.ebi.ac.uk/Tools/msa/clustalo/). To predict the similarities between the secondary structures of Moh1p and YPEL2, we used the jPred4 [45] server (http://www.compbio.dundee.ac.uk/jpred4/index.htmL). For the tertiary structure prediction and superimposition of the tertiary structures of Moh1p and YPEL2, we used the AlphaFold [46, 47] server (https://alphafold.ebi.ac.uk/) with the ChimeraX molecular visualization [48, 49] program (https://www.cgl.ucsf.edu/chimerax/). For the homology modeling f YPEL2 and Moh1 proteins, we used Phyre2 [50] web tool (http://www.sbg.bio.ic.ac.uk/~phyre2/htmL/page.cgi?id=index).

Yeast strains and growth conditions

Strains that are used in this study are given in **Table 1**. *S.cerevisiae* BY4741 (*MATa, his3Δ1, leu2Δ0, met15Δ0, ura3Δ0*) strain as the wild-type strain (WT) and BY4741 *MOH1* knockout mutant strain (*moh1Δ; MATa, his3Δ1, leu2Δ0, met15Δ0, ura3Δ0, Moh1Δ::KanMX4*) were purchased from Dharmacon (HorizonDiscovery Inc., UK). For the growth of cell strains, we used a yeast extract-peptone-dextrose (YPD) medium containing 1% yeast extract (Sigma, Germany, 70161), 2% dextrose (Sigma, Germany, 49159), and 2% peptone (Sigma, Germany, 912489). For the colony selection after transformation, we used a synthetic complex medium without uracil (SC-URA) that contains 0.67% yeast nitrogen base without amino acids (Sigma, Germany, Y0626), 2% dextrose, and 0.192% yeast synthetic drop-out medium supplements without uracil and YPD with 5-FOA (1 mg/mL 5-FOA; F9001, Zymo Research, USA).

To induce stress, we used two conditions: short-term and long-term. In the short-term stress condition, cells were grown overnight in YPD at 30°C with shaking at 180 rpm. Cells in log phase were then subcultured into fresh YPD at a 1:100 dilution and grown at 30°C until the OD_{600} reached 0.4–0.6. A stress inducer was added to the medium, and cells were incubated for 45 minutes. Cells were harvested by centrifugation, pelleted, and processed for subsequent experiments. For the long-term stress condition, the autoclaved YPD-Agar medium was cooled down to 55°C, and a stress inducer was added to stress agar plates. For spot tests, cells grown overnight in YPD at 30°C with shaking at 180 rpm were sub-cultured into fresh YPD at a 1:100 dilution and grown until OD_{600} reached 0.4. Cells were subsequently spotted at serial dilution on agar plates containing a stress inducer, and the plates were incubated at 30°C for 40 hours. Cells were then collected with a scraper into sterile water and pelleted for subsequent experimental procedures.

As stress inducers, we used sulfuric acid (Merck, Germany, 1.00713), hydrogen peroxide (Merck, Germany, 107209), acetic acid (Sigma, Germany, A6283), and sodium azide (Sigma, Germany, S2002) by adding them to YPD medium.

Establishment of yeast strains

Cloning into the upstream and downstream homology arms of the pBS-KS(-) vector

The *moh1Δ* yeast strain contains the KanMX4 selector module in the *MOH1* locus. For the generation of the *moh-i* or *f-moh-i* strain, we initially replaced the KanR gene in the KanMX selector module with *URA3* (orotidine-5′ -phosphate decarboxylase) as the selector module in the *moh1Δ* strain. To accomplish this, we initially cloned the upstream (UPS) and downstream (DNS) homology arms (about 200 bp) of the KanR gene generated by PCR using the *moh1Δ* genomic DNA as the template and specific primer sets (Supplementary Information Table S5) with restriction enzyme sites into the pBS-KS(-) vector to generate pBSKS-UPS-DNS. We subsequently inserted the URA3 gene generated with PCR by using the pRS314-URA3 vector (a gift from Francisco Malagon; Addgene plasmid #11004; http://n2t.net/addgene:11004; RRID: Addgene_11004) DNA as the template and URA3-specific primers with restriction enzyme sites into pBSKS-UPS-DNS to obtain the pBSKS-UPS-URA3-DNS vector.

Insertion into the yeast genome

For the insertion of the UPS-URA3-DNS selector module into the *moh1Δ* genome, the UPS-URA3-DNS DNA fragment generated with PCR using pBSKS-UPS-URA3-DNS as the template was transformed into the *moh1Δ* strain for homologous recombination. For transformation, a single colony of the *moh1Δ* strain was grown in YPD overnight at 30°C with shaking at 180 rpm. The overnight culture was then subcultured into fresh YPD at a 1:100 dilution and grown until OD_{600} reached 0.4–0.6. Cells were pelleted at 4000 rpm for 5 minutes and washed with sterile distilled water. After centrifugation, cells were resuspended in 0.1 M LiAc solution and centrifuged at 12000 rpm for 10 seconds. The cell pellet was resuspended in 0.1 LiAc solution and placed on ice. Single-stranded salmon sperm DNA (ssDNA) was

TABLE 1 ● **Cell strains used in this study** .

Name	Genotype	Abbrevation	Source
BY4741	MATa *his3Δ1 leu2Δ0 met15Δ0 ura3Δ0*	WT	Dharmacon
moh1Δ-BY4741	BY474 *moh1Δ::KanMX4*	*moh1Δ*	Dharmacon
moh1Δ-BY4741+*URA3*	BY4741 *moh1Δ::URA3*	*ura3-i*	This study
moh1Δ-BY4741+*WT-MOH1*	BY4741 *moh1Δ::MOH1*	*moh1-i*	This study
moh1Δ-BY4741+*flag-MOH1*	BY4741 moh1Δ::flag-MOH1	*f-moh1-i*	This study

boiled at 98°C for 10 minutes and incubated on ice for 10 minutes. The transformation was carried out by sequential addition of 50% (w/v) PEG (Sigma, Germany, 202444), 1 M LiAc, 2 mg/mL ssDNA, the PCR product, and the cell suspension in a fresh tube and vortexing it for 2 minutes. The suspension was then plated onto SC-URA plates, and cells were grown at 30°C for 3 days for colony formation.

Screening of transformants

Single colonies were placed into SC-URA selective medium to screen transformants. Overnight-grown cells were centrifuged, and the cell pellet was resuspended in yeast lysis buffer containing 10 mM Tris (pH = 8), 0.2% Triton X-100, 1% SDS, 100 mM NaCl, and 1 mM EDTA. Phenol:chloroform:isoamyl alcohol (25:24:1, basic) and acid-washed glass beads (Sigma, Germany, G9268) were added to resuspended cells. The mixture was vortexed for 4 minutes. Tris-EDTA (TE) buffer was added to the mixture and was centrifuged at 6500 rpm for 2 minutes. The aqueous phase was transferred into a new centrifuge tube and washed with 100% ethanol. DNA was pelleted by centrifugation at 12000 rpm for 2 minutes. The pellet was dissolved in TE buffer, precipitated with ethanol and 3 M ammonium acetate. The genomic DNA pellet was air-dried for 15 minutes and resuspended in water. The genomic DNA was used for PCR with primer sets specific to (1) KanR, (2) URA3, (3) URA3 and upstream sequences of the UPS homology arm in the genome, (4) sequences at the upstream and downstream of UPS and DNS homology arms, respectively, in the genome (Supplementary Information Fig. S9A, S9B and Table S5). After PCR confirmation, samples were sequenced to verify PCR results.

Insertion of the WT-MOH1 or Flag-MOH1 gene into the yeast genome

To generate yeast strains bearing WT-*MOH1* (*moh1-i*) or *Flag-MOH1* (f-moh1-i), we used the same procedure to generate *moh1Δ* with *URA3* as described above, such that genes with upstream and downstream homology arms of the *MOH1* locus were amplified with PCR. Amplicons were then transformed into the *ura3-i* strain as described above. Cell suspensions were then plated onto YPD. After one day of growth, plates were replica-plated onto YPD containing 5-fluoroorotic acid [145] and placed in a 30°C incubator for three days for colony formation. Following PCR screening of transformants with primers specific to the gene of interest and homology arms as described above (Supplementary Information Fig. S9C, S9D and Table S5), positive transformants were subjected to sequencing.

Growth in water

A single colony from WT, *moh1Δ*, *moh1-i*, and *f-moh1-i* strains was grown in YPD overnight. 50 × 10^6 cells were subcultured into fresh YPD and grown for one week. After one week of growth, cells were washed twice with 1 M Sorbitol (Sigma, Germany, S1876) and once with sterile distilled water. Cells were then resuspended with 20 mL of sterile distilled water and incubated at 30°C and 180 rpm for up to 18 days. Every second day, aliquots from these water cultures were collected for a spot test, for which 10-fold serial dilutions from each aliquot were spotted on the YPD-Agar plate. Cells were incubated at 30°C for 40 hours and photographed with the ChemiDoc™ MP System (BioRad, USA).

Growth under stress conditions

A single colony from WT, *moh1Δ*, *moh1-i*, and *f-moh1-i* strains grown in YPD overnight was subcultured into 20 mL of YPD at a ratio of 1:100. Cells were grown until OD_{600} reached 0.4–0.6. Cells were counted, and 2.5 × 10^6 cells/mL was used for 10-fold serial dilutions for spotting on stress agar plates as described above. Similarly cells were spotted on stress agar plates containing none, or 25–100 μg/mL Congo red (MedChemExpress, USA, HY-D0236) or 0.005–0.01% SDS (Sodium Dodecyl Sulfate, Sigma-Aldrich, Germany, A, L3771). Plates were incubated at 30 °C for 40 hours. The spots on the plates were photographed with the ChemiDoc™ MP system (Bio-Rad, USA).

To assess the effects of nutritional adjustments under different temperature or pH on the growth of WT and *moh1Δ* cells, 2.5 × 10^6 cells/mL, with 10-fold serial dilutions (black triangles), were spotted onto the indicated agar (2%) plates: YPD (1% Yeast extract, 2% Peptone, 2% Dextrose), YPRG (1% Yeast extract, 2% Peptone, 3% Raffinose, and 2% Galactose), Glycerol (1% Yeast extract, 2% Peptone, 3% Glycerol), or low glucose (1% Yeast extract, 2% Peptone, 0.5% or 1% Glucose). Plates were incubated at 23, 30, 33, 35, and 37 °C for 40 hours and photographed.

For spot tests at different pH, buffered YPD agar plates prepared YPD-agar base (1% yeast extract, 2% peptone, 2% dextrose and 2% agar), sterilized by autoclaving. The molten medium was then supplemented with sterile buffer to the indicated pH while maintaining a constant final buffer strength (~50 mM) across conditions. For pH 6–8, a citrate-phosphate system was used by combining citric acid with Na_2HPO_4 at pH-specific ratios to achieve the target pH. Plates were incubated at 30°C for 40 hours and photographed.

Western Blot (WB)

Cells subjected to either long-term or short-term stress were collected and counted. 500 × 10^6 cells were pelleted in centrifuge

tubes. After washing the pellets with sterile distilled water, the cells were resuspended in 75 μL of urea-lysis buffer (40 mM Tris, pH 6.8; 0.1 mM EDTA; 5% SDS; 9 M urea; 0.02 mg/mL bromophenol blue) and mixed with 75 μL of glass beads. The mixture was vortexed five times for 1 minute each, with 1-minute ice breaks between vortexes. Using a heated syringe needle, the bottom of the tube was punctured and the contents transferred to a clean tube, then centrifuged at 4000 rpm for 2 minutes to remove glass beads. The mixture was centrifuged at 14,000 rpm for 15 minutes, and the supernatant was transferred to a clean tube. Equal volumes (25 μL) of supernatant from each sample were loaded onto a 10% SDS-PAGE gel for WB analysis. After transferring proteins to a PVDF membrane (Advansta, WesternBrightTM PVDF-CL, L-08008-001) via wet transfer, the membrane was blocked with 5% skim milk in 0.1% Tris-buffered saline-Tween (TBS-T). Proteins were detected using a Flag Antibody (1:1000 dilution; M2-Flag, Sigma-Aldrich, F-1804). Specificity of detection of flag-Moh1 with the Flag antibody was initially assessed in COS7 cells, an African green monkey kidney fibroblast-like cell line as we described previously [30], which were transiently transfected with the expression vector bearing none (Vector control), MOH1 or Flag-MOH1 cDNA for 24 h (Supplementary Infomation, Fig. S12). Following three 5-minute washes with 0.1% TBS-T, the membrane was incubated with a goat anti-mouse HRP-conjugated secondary antibody (1:4000 dilution in 5% skim milk in 0.1% TBS-T, Santa Cruz Biotechnology, USA) for 1 hour at room temperature. The membrane was then treated with WesternBright ECL substrate (Advansta, K-12045-D50) in a 1:1 ratio of luminol-enhancer reagent to peroxide reagent in the dark for 2 minutes to detect proteins. The ChemiDocTM MP system (Bio-Rad, USA) was used for visualization.

RNA isolation and RT-qPCR

Cells subjected to long- or short-term stress were collected and pelleted in centrifuge tubes. To dissolve cell pellets, 25 μL of 20% SDS and 400 μL of ice-cold Acetate-EDTA (AE) buffer containing 50 mM sodium acetate and 10 mM EDTA (pH = 8) were added to the cell pellets. Subsequently, 500 μL of acidic 25:24:1 phenol:chloroform:isoamyl alcohol (PCI) solution was added to the cell suspension. The cell suspension was incubated at 65°C for 15 minutes, followed by incubation on ice for 10 minutes. For phase separation, samples were centrifuged at 14000 rpm at 4°C for 15 minutes, and the liquid phase was transferred to a sterile tube containing 500 μL of PCI. The mixture was vortexed for 20 seconds and incubated on ice for 10 minutes. After centrifugation of the samples at 14,000 rpm for 15 minutes at 4°C, the supernatant was transferred to a new sterile tube, followed by the addition of one-tenth volume of sodium acetate (pH 5.3) and three volumes of 100% ethanol. Samples were incubated at −80°C for 30 minutes. RNA was precipitated by centrifugation at 14000 rpm at 4°C for 15 minutes and dissolved in diethylpyrocarbonate (DEPC)-treated water. RNA samples were also treated with DNase I to degrade any remaining DNA. The purity and concentration of RNA were determined using a Nanodrop 2000 spectrophotometer (Thermo-Fisher Sci., California, USA) with A260/A280 and A260/A230 ratios. Isolated RNAs were used for cDNA synthesis (The RevertAid First Strand cDNA Synthesis Kit, Thermo-Fisher) with oligo $(dT)_{18}$ primers according to the manufacturer's instructions. qPCR experiments were carried out with SsoAdvanced Universal SYBR Green SuperMix (Bio-Rad, USA) and transcript variant-specific primers. *YPR062W* (*FCY1*) and *YNL219C* (*ALG9*) were used as reference genes for normalization in the analyses, and the differential expression was shown as fold change using the $2^{-\Delta\Delta C_T}$ approach [146]. RT-qPCR experiments were performed with the MIQE Guidelines [147].

Scanning Electron Microscopy (SEM)

Samples were prepared and analyzed using SEM at the Prof. Dr. Zekiye Suludere Electron Microscope Center, Gazi University, Ankara, Türkiye. For SEM analysis, WT, *moh 1Δ*, and *moh 1-i* cells were cultured under logarithmic phase, stationary phase, and solid-growth conditions. A single colony was initially inoculated into YPD medium and incubated overnight at 30°C with reciprocal shaking at 180 rpm. To obtain cells in the logarithmic phase, cultures were diluted 1:100 and grown at 30°C with reciprocal shaking at 180 rpm until reaching an OD_{600} of 0.4–0.6. At this point, half of the culture was subjected to short-term H_2O_2 stress for 45 min while the other half served as the control. For the stationary phase, after subculturing, cells were grown for 48 hours at 30°C with reciprocal shaking at 180 rpm. This was followed by short-term H_2O_2 stress for 45 minutes, while the other half served as the control. For cells in the logarithmic and stationary phases, cultures were collected, washed twice with sterile water, and centrifuged at 1,000 rpm for 3 minutes. The resulting cell pellets were resuspended in 4% glutaraldehyde for fixation. To prepare solid cultures, cells from the logarithmic phase were counted using a hemocytometer, and 250 cells were plated on YPD-Agar plates with or without H_2O_2. Plates were incubated for 40 hours at 30°C. From these plates, small sections containing yeast colonies were excised and transferred into vials containing 4% glutaraldehyde in water for fixation. After fixation, cells were rinsed with water. Fixed cells were dehydrated using an ascending series of ethanol (70%, 80%, 90%, and 100%) and then air-dried. The samples were treated with amyl acetate, followed by critical point drying using a Polaron CPD 7501 (Quorum Technologies, UK) under liquid carbon dioxide. Samples were coated with gold using a Polaron SC 502 sputter coater (Quorum Technologies, UK). Imaging was performed with a HITACHI SU 5000 Schottky Field Emission Scanning Electron Microscope (FE- SEM, HITACHI, Japan).

RNA sequencing

RNA-Seq analysis

Two μg of RNA extracted from WT and *moh1Δ* cells in spot tests, as described above, were used for sequencing. For RNA sequencing, RNA-Seq libraries were prepared with the BGISEQ-500 sequencing platform (Genoks, Ankara, Türkiye, through BGI Genomics, Shenzhen, People's Republic of China) with a 100 bp paired-end sequencing approach and a sequencing depth of at least 30 million [148, 149]. Results obtained after the sequencing were subjected to quality control. Contaminations in the read data, adapter sequences, sequences shorter than 30 bases, and low-quality readings were filtered out. The clean

readings obtained after filtering were aligned to the latest *S. cerevisiae* genome (Ensemble 101) using STAR (Hierarchical Indexing for Spliced Alignment of Transcripts) software [150]. Transcript and gene count matrices were obtained with featureCounts [151] after the alignment process. The RNA-Seq data generated in this study have been deposited in the ArrayExpress database (https://www.ebi.ac.uk/arrayexpress/) under accession number E-MTAB-16090. The count data were used to analyze differentially expressed genes (DEGs) using DeSeq2. For the DeSeq2, WT cells were used as the reference. Genes with an adjusted p-value < 0.05 and a $\log_2$ fold change greater than ± 0.6 were considered differentially expressed. After DeSeq2 analysis, DEGs were listed for each group, and pathway analyses were performed. All analyses were conducted using the R language. We utilized the Metascape portal ([72] https://metascape.org/) using a P-value of 0.05 as the threshold.

Verification of RNA-Seq results with RT-qPCR

RNA samples reserved before RNA sequencing were used for the construction of cDNA libraries using the RevertAid First Strand cDNA Synthesis Kit (Thermo-Fisher) with oligo (dT)18 primers according to the manufacturer's instructions. *ALD3, GRE1,* and *SRL1*, identified as differentially expressed genes and selected based on their cellular functions, were chosen to verify the RNA-Seq results. RT-qPCR experiments were carried out as described in Section 2.4 using transcript-specific primer sets (Supplementary Information Table S5).

Fourier Transform-Infrared Spectroscopy (FTIR)

WT and *moh1Δ* strains were cultured overnight in YPD medium at 30°C with shaking at 180 rpm. After overnight growth, cells were diluted 1:100 into fresh YPD medium. Cells grown to an OD_{600} of 0.4–0.6 were spotted on YPD-agar plates and incubated at 30°C for 40 hours. Cells were scraped from the agar plate, placed in sterile distilled water, and centrifuged at 1000 rpm for 5 minutes. The cells were washed once with distilled water, and 20×10^7 were resuspended in 5 µL of water. Five biological replicates of WT and *moh1Δ* cells were prepared for FTIR analysis.

FTIR readings were conducted at the East Anatolia High Technology Application and Research Center of Atatürk University in Erzurum, Türkiye, using the Attenuated Total Reflectance (ATR) mode of FTIR spectroscopy (Bruker Vertex 70, Ettlingen, Germany). To prepare samples, 3 µL of concentrated yeast was placed on an ATR crystal, and cells were dried with N_2 gas for 5 minutes. For each group, five spectra were collected with two technical replicates. Spectra were acquired with 32 scans over the 4000–400 cm^{-1} spectral range at a spectral resolution of 4 cm^{-1} using OPUS 7.5 (Bruker, Ettlingen, Germany) software. After each measurement, the diamond crystal was cleaned with 70% ethanol and distilled water.

For qualitative and quantitative spectral analysis, all data manipulation and calculations to determine band intensity values, bandwidth, and band positions were performed using OPUS 5.5 software (Bruker Optics, Reinstetten, Germany). Quantitative band intensity (I) calculations were performed using concave rubber band baseline correction (iteration: 15; number of iterations: 128) on spectra over the entire spectral range for all samples. Band intensity ratios were used to estimate the relative concentrations of individual biomolecules within the system. When broad bands have bandwidths exceeding the separation between adjacent peaks, techniques such as Fourier deconvolution, second derivative analysis, and curve fitting are suitable for resolution enhancement [77]. In this study, second-derivative analysis was applied to the spectral range of 1185–930 cm^{-1} to assess the contributions of mannan and glucan components. Spectral parameters related to lipid order and membrane fluidity were determined from the frequency and bandwidth of the CH_2 asymmetric band. To investigate variations in protein secondary structures, we also used the second derivative method [152, 153]. This process began with a concave rubber band baseline correction (15 iterations; number of iterations: 128) across the full spectral range, followed by vector normalization within 1700–1600 cm^{-1}. Second derivative spectra were then obtained using the Savitzky-Golay algorithm (9 smoothing points) in OPUS 5.5 software (Bruker Optics, Reinstetten, Germany). The characteristic minima in these second derivative spectra correspond to secondary protein structures: α-helices (1654 cm^{-1}), β-sheets (1639 cm^{-1}), and β-turns (1689 cm^{-1}) [154, 155]. Changes in the intensity of these amide I bands in the second-derivative spectra reflect the relative proportions of secondary structural components of proteins.

Chemometric analyses, including principal component analysis (PCA) and hierarchical cluster analysis (HCA), were performed using the Unscrambler X software package (version 10.4, CAMO Software, Oslo, Norway) on spectra that had been baseline-corrected with concave rubber band correction (iteration: 15; iteration number: 128) and vector-normalized within the 4000–400 cm^{-1} spectral range. PCA was applied to the preprocessed spectra across the entire spectral region (4000–400 cm^{-1}) to identify differences between WT and *moh1Δ* cells. The analysis used mean-centered data, full cross-validation, and the singular value decomposition (SVD) algorithm. Results were displayed as PCA score plots. To support the PCA findings, HCA was performed using Ward's linkage algorithm combined with squared Euclidean distance measurements. The clustering results were visualized with a dendrogram.

A student's t-test was performed using GraphPad Prism 8.0 statistics software (GraphPad, La Jolla, CA) for the statistical significance of the quantitative spectral data. The results are presented as the mean ± S.E.M., and values less than or equal to 0.05 were considered statistically significant for comparisons, $*p \leq 0.05$; $**p \leq 0.01$, $***p \leq 0.001$).

Catalase activity assay

WT and *moh1Δ* strains, cultured overnight in YPD at 30°C with shaking at 180 rpm, were diluted 1:100 into fresh YPD and grown to OD_{600} = 0.4–0.6. Cultures were split into five aliquots; one was used as an untreated control, and the others were exposed to 0.325, 0.650, 1.3, or 3.25 mM H_2O_2 for 45 min. Cells were harvested, washed with 100 mM potassium phosphate (pH 7.0) containing 0.1 mM PMSF. Cells were resuspended in 200 µL of

the same buffer and disrupted with an equal volume of acid-washed glass beads by four cycles of 45 seconds of vortexing and 45 seconds of cooling on ice. Lysates were clarified by centrifugation (13,000 × g, 10 min, 4°C), and the supernatants were used as crude protein extracts.

From these crude extracts, 60–100 µL (minimum of 80 µg protein) of the sample was added to 2 mL of 20 mM H_2O_2 in 50 mM KPi buffer (pH 7.0), and H_2O_2 decomposition was monitored at 240 nm (ε_{240} = 43.6 M^{-1} cm^{-1}) for 1 minute. For the catalase activity calculation, the following formulation was used:

$$\frac{\Delta OD_{240}/\text{ min} * Volume_{Total} * 10^6}{\varepsilon_{240} * l * Protein\ mass\ (mg)}$$

$\Delta OD_{240}/$ min : the rate of decrease in absorbance at 240 nm per minute

$Volume_{Total}$: total reaction volume (L)

ε_{240} : molar extinction coefficient of H_2O_2 (43.6 M^{-1} cm^{-1})

l : path length (1 cm)

Protein mass(*mg*) : total protein amount present in the assay

Catalase activity results are expressed as the fold change of the mean ± S.E.M. from three independent cultures, with comparisons considered statistically significant at $p \leq 0.05$.

Flow cytometry analysis

2′, 7 ′- Dichlorofluorescin diacetate (H_2DCFDA or DCFDA) is a widely used fluorometric probe for detecting reactive oxygen species (ROS) within cells. H_2DCFDA is a non-fluorescent, lipophilic, and cell membrane-permeable compound [114]. It is recognized as a general ROS indicator, reacting with various species including hydroxyl and peroxyl radicals, peroxynitrite, and lipid hydroperoxides [114]. Once inside the cell, H_2DCFDA becomes fluorescent upon oxidation by cellular ROS, enabling the detection of intracellular ROS. For ROS detection with H_2DCFDA, we used WT and *moh1Δ* cells. A single colony was inoculated into YPD medium and incubated overnight at 30 °C with shaking at 180 rpm. To obtain cells in the logarithmic phase, the overnight culture was diluted 1:100 in fresh YPD and further incubated under the same conditions until OD_{600} reached 0.4–0.6. The culture was then divided into three equal parts: one received a treatment of 3.25 mM H_2O_2 for 45 minutes to induce short-term oxidative stress; another was treated with 25 µg/mL Antimycin A (Sigma, Germany, A 8674) for 45 minutes to stimulate mitochondrial ROS production as a positive control. The remaining part was left untreated as a control. After incubation with none, H_2O_2, or Antimycin A, each culture was split into two equal parts and transferred into microfuge tubes. One-half was incubated with 20 µM H_2DCFDA (MedChemExpress, USA, HY-D 0940) for 45 minutes at 30°C in the dark to detect ROS accumulation. The other half was left untreated to serve as an unstained control. Following staining, cells were washed twice with PBS by centrifugation at 6000 × g for 3 minutes. Fluorescence intensity was then measured using a BD Accuri C6 Plus Flow Cytometer (BD Biosciences, USA). Since H_2DCFDA fluoresces upon oxidation with excitation at 488 nm and emission at 525 nm, the FL1-A channel was used for detection. A minimum of 100,000 events was recorded per sample. A sample gating strategy is provided in Supplementary Information Fig. S10. Data acquisition and analysis were performed using BD Accuri C6 software (BD Biosciences, USA).

AUTHORS CONTRIBUTIONS

Çağla Ece Olgun and Gizem Turan Duman have contributed equally.

Çağla Ece Olgun: conceptualization, data curation, formal analysis, investigation, funding acquisition, methodology, writing original draft, and editing.

Gizem Turan Duman: data curation, investigation, methodology, writing original draft, and editing.

Gizem Güpür: data curation, investigation, methodology, writing original draft, and editing.

Hamit İzgi: RNA-Seq Analysis

Mariam Huda: methodology

Demet Çetin: Scanning Electron Microscopy Analysis

Zekiye Suludere: Scanning Electron Microscopy Analysis

Fatma Küçük Baloğlu: FTIR analysis

Ayşe Koca Çaydaşı: methodology, formal analysis, writing original draft, and editing

Mesut Muyan: conceptualization, data curation, formal analysis, supervision, funding acquisition, methodology, writing original draft, editing, and project administration.

ACKNOWLEDGEMENTS

This research was supported by ODTÜ-ÇDAP-108-2023-11112 (MM), TUBITAK-1001-117Z213 (MM), TUBITAK-1002-119Z570 (ÇEO), and TUBITAK-1002-124Z032 (ÇEO). We thank TUBITAK for their support. We are grateful to Drs. Mark Dumont, Cory Dunn, Ahmet Koç, Nihal Terzi Çizmecioğlu, and Çağdaş Devrim Son for their scientific and technical guidance. We thank Dr. Nihal Şimşek Özek, Atatürk University, Erzurum, Türkiye, for performing FTIR measurements. We thank the members of the Muyan laboratory for their stimulating discussions, contributions, and critical review of the manuscript.

SUPPLEMENTAL MATERIAL

All supplemental data for this article are available online at www.microbialcell.com.

CONFLICT OF INTEREST

The authors declare no conflict of interest.

Please cite this article as: Çağla Ece Olgun, Gizem Turan Duman, Gizem Güpür, Hamit İzgi, Mariam Huda, Demet Çetin, Zekiye Suludere, Fatma Küçük Baloğlu, Ayşe Koca Çaydaşı, Mesut Muyan (**2026**). Yippee-like protein Moh1 links gene expression to metabolism and selective stress resistance in *Saccharomyces cerevisiae*. **Microbial cell** 13: 261-281. doi: 10.15698/mic2026.06.881

REFERENCES

1. Roxström-Lindquist K, Faye I (**2001**). The *Drosophila* gene *Yippee* reveals a novel family of putative zinc binding proteins highly conserved among eukaryotes. **Insect Mol Biol** 10 (1): 77–86. doi:10.1046/j.1365-2583.2001.00239.x
2. Hosono K, Sasaki T, Minoshima S, Shimizu N (**2004**). Identification and characterization of a novel gene family YPEL in a wide spectrum of eukaryotic species. **Gene** 340 (1): 31–43. doi:10.1016/j.gene.2004.06.014
3. Hosono K, Noda S, Shimizu A, Nakanishi N, Ohtsubo M, Shimizu N, Minoshima S (**2010**). YPEL5 protein of the YPEL gene family is involved in the cell cycle progression by interacting with two distinct proteins RanBPM and RanBP10. **Genomics** 96 (2): 102–111. doi:10.1016/j.ygeno.2010.05.003
4. Tuttle R, Miller KR, Maiorano JN, Termuhlen PM, Gao Y, Berberich SJ (**2012**). Novel senescence associated gene, *YPEL3*, is repressed by estrogen in ER+ mammary tumor cells and required for tamoxifen-induced cellular senescence. **Int J Cancer** 130 (10): 2291–2299. doi:10.1002/ijc.26239
5. Nott SL, Huang Y, Li X, Fluharty BR, Qiu X, Welshons WV, Yeh S, Muyan M (**2009**). Genomic Responses from the Estrogen-responsive Element-dependent Signaling Pathway Mediated by Estrogen Receptor α Are Required to Elicit Cellular Alterations. **J Biol Chem** 284 (22): 15277–15288. doi:10.1074/jbc.M900365200
6. Aerts S, Lambrechts D, Maity S, Van Loo P, Coessens B, De Smet F, Tranchevent L-C, De Moor B, Marynen P, Hassan B, Carmeliet P, Moreau Y (**2006**). Gene prioritization through genomic data fusion. **Nat Biotechnol** 24 (5): 537–544. doi:10.1038/nbt1203
7. Farlie P, Reid C, Wilcox S, Peeters J, Reed G, Newgreen D (**2001**). Ypel1: a novel nuclear protein that induces an epithelial-like morphology in fibroblasts. **Genes Cells** 6 (7): 619–629. doi:10.1046/j.1365-2443.2001.00445.x
8. Tan TY, Gordon CT, Miller KA, Amor DJ, Farlie PG (**2015**). *YPEL1* overexpression in early avian craniofacial mesenchyme causes mandibular dysmorphogenesis by up-regulating apoptosis. **Dev Dyn** 244 (8): 1022–1030. doi:10.1002/dvdy.24299
9. S Ruiz García, Deprez M, Lebrigand K, Cavard A, Paquet A, Arguel M-J, Magnone V, Truchi M, Caballero I, Leroy S, Marquette C-H, Marcet B, Barbry P, Zaragosi L-E (**2019**). Novel dynamics of human mucociliary differentiation revealed by single-cell RNA sequencing of nasal epithelial cultures. **Development** 146 (20). doi:10.1242/dev.177428
10. Li W, Huang W, Wu K, Long Y (**2022**). Yippee Like 1 Suppresses Glioma Progression and Serves as a Novel Prognostic Factor. **Tohoku J Exp Med** 256 (2): 141–150. doi:10.1620/tjem.256.141
11. Baker SJ (**2003**). Small unstable apoptotic protein, an apoptosis-associated protein, suppresses proliferation of myeloid cells. **Cancer Res** 63 (3): 705–712, PMID: 12566317
12. Kelley KD, Miller KR, Todd A, Kelley AR, Tuttle R, Berberich SJ (**2010**). YPEL3, a p53-Regulated Gene that Induces Cellular Senescence. **Cancer Res** 70 (9): 3566–3575. doi:10.1158/0008-5472.CAN-09-3219
13. Zhang J, Wen X, Ren X-Y, Li Y-Q, Tang X-R, Wang Y-Q, He Q-M, Yang X-J, Sun Y, Liu N, Ma J (**2016**). YPEL3 suppresses epithelial–mesenchymal transition and metastasis of nasopharyngeal carcinoma cells through the Wnt/β-catenin signaling pathway. **J Exp Clin Cancer Res** 35 (1): 109. doi:10.1186/s13046-016-0384-1
14. Blanco-Sánchez B, Clément A, Stednitz SJ, Kyle J, Peirce JL, McFadden M, Wegner J, Phillips JB, Macnamara E, Huang Y, Adams DR, Toro C, Gahl WA, Malicdan MC V, Tifft CJ, Zink EM, Bloodsworth KJ, Stratton KG, Koeller DM, Metz TO, Washbourne P, Westerfield M (**2020**). Yippee like 3 (ypel3) is a novel gene required for myelinating and perineurial glia development. **PLoS Genet** 16 (6): e1008841. doi:10.1371/journal.pgen.1008841
15. Baek H-S, Kwon T-U, Shin S, Kwon Y-J, Chun Y-J (**2021**). Steroid sulfatase deficiency causes cellular senescence and abnormal differentiation by inducing Yippee-like 3 expression in human keratinocytes. **Sci Rep** 11 (1): 20867. doi:10.1038/s41598-021-00051-w
16. Kim JH, Singh M, Pan G, Lopez A, Zito N, Bosse B, Ye B (**2020**). Frameshift mutations of *YPEL3* alter the sensory circuit function in *Drosophila*. **Dis Model Mech** 13 (6): dmm042390. doi:10.1242/dmm.042390
17. Kong X, Li Y, Zhang X (**2018**). Increased Expression of the YPEL3 Gene in Human Colonic Adenocarcinoma Tissue and the Effects on Proliferation, Migration, and Invasion of Colonic Adenocarcinoma Cells In Vitro via the Wnt/b-Catenin Signaling Pathway. **Med Sci Monit** 24: 4767–4775. doi:10.12659/MSM.908173
18. Liang P, Wan Y, Yan Y, Wang Y, Luo N, Deng Y, Fan X, Zhou J, Li Y, Wang Z, Yuan W, Tang M, Mo X, Wu X (**2010**). MVP interacts with YPEL4 and inhibits YPEL4-mediated activities of the ERK signal pathway. **Biochem Cell Biol** 88 (3): 445–450. doi:10.1139/O09-166
19. Mattebo A, Sen T, Jassinskaja M, Pimková K, Prieto González-Albo I, Alattar AG, Ramakrishnan R, Lang S, Järås M, Hansson J, Soneji S, Singbrant S, van den Akker E, Flygare J (**2021**). Yippee like 4 (Ypel4) is essential for normal mouse red blood cell membrane integrity. **Sci Rep** 11 (1): 15898. doi:10.1038/s41598-021-95291-1
20. Oki K, Plonczynski MW, Gomez-Sanchez EP, Gomez-Sanchez CE (**2016**). YPEL4 modulates HAC15 adrenal cell proliferation and is associated with tumor diameter. **Mol Cell Endocrinol** 434: 93–98. doi:10.1016/j.mce.2016.06.022
21. Jun D-Y, Park H-W, Kim Y-H (**2007**). Expression of Yippee-Like 5 (YPEL5) Gene During Activation of Human Peripheral T Lymphocytes by Immobilized Anti-CD3. **J Life Sci** 17 (12): 1641–1648. doi:10.5352/JLS.2007.17.12.1641
22. Lee JY, Jun DY, Park JE, Kwon GH, Kim J-S, Kim YH (**2017**). Pro-Apoptotic Role of the Human YPEL5 Gene Identified by Functional Complementation of a Yeast *moh1Δ* Mutation. **J Microbiol Biotechnol** 27 (3): 633–643. doi:10.4014/jmb.1610.10045
23. Wu X (**2018**). Up-regulation of YPEL1 and YPEL5 and down-regulation of ITGA2 in erlotinib-treated EGFR-mutant non-small cell lung cancer: A bioinformatic analysis. **Gene** 643: 74–82. doi:10.1016/j.gene.2017.12.003
24. Li S, Sun M-Y, Su X (**2019**). MiR-885-5p promotes gastric cancer proliferation and invasion through regulating YPEL1. **Eur Rev Med Pharmacol Sci** 23 (18): 7913–7919. doi:10.26355/eurrev_201909_19005
25. Vysotskiy M, Zhong X, Miller-Fleming TW, Zhou D, Cox NJ, Weiss LA (**2021**). Integration of genetic, transcriptomic, and clinical data provides insight into 16p11.2 and 22q11.2 CNV genes. **Genome Med** 13 (1): 172. doi:10.1186/s13073-021-00972-1
26. Tuttle R, Simon M, Hitch DC, Maiorano JN, Hellan M, Ouellette J, Termuhlen P, Berberich SJ (**2011**). Senescence-Associated Gene YPEL3 Is Downregulated in Human Colon Tumors. **Ann Surg Oncol** 18 (6): 1791–1796. doi:10.1245/s10434-011-1558-x
27. Li Y, Wang Z, Wu X, Wang G, Gu G, Ren H, Hong Z, Ren J (**2021**). Intestinal mucosa-derived DNA methylation signatures in the penetrating intestinal mucosal lesions of Crohn's disease. **Sci Rep** 11 (1): 9771. doi:10.1038/s41598-021-89087-6
28. de Bruijn SE, et al. (**2020**). Structural Variants Create New Topological-Associated Domains and Ectopic Retinal Enhancer-Gene Contact in Dominant Retinitis Pigmentosa. **Am J Hum Genet** 107 (5): 802–814. doi:10.1016/j.ajhg.2020.09.002
29. Mascia F, Mazo I, Alterovitz W-L, Karagiannis K, Wu WW, Shen R-F, Beaver JA, Rao VA (**2022**). In search of autophagy biomarkers in breast cancer: Receptor status and drug agnostic transcriptional changes during autophagy flux in cell lines. **PLoS One** 17 (1): e0262134. doi:10.1371/journal.pone.0262134
30. Turan G, Olgun ÇE, Ayten H, Toker P, Ashyralyyev A, Savaş B, Karaca E, Muyan M (**2024**). Dynamic proximity interaction profiling suggests that

YPEL2 is involved in cellular stress surveillance. **Protein Sci** 33 (2): e4859. doi:10.1002/pro.4859

31. Mohammadi S, Saberidokht B, Subramaniam S, Grama A (**2015**). Scope and limitations of yeast as a model organism for studying human tissue-specific pathways. **BMC Syst Biol** 9 (1): 96. doi:10.1186/s12918-015-0253-0
32. Ashrafi K, Farazi TA, Gordon JI (**1998**). A role for Saccharomyces cerevisiae fatty acid activation protein 4 in regulating protein N-myristoylation during entry into stationary phase. **J Biol Chem** 273 (40): 25864–25874. doi:10.1074/jbc.273.40.25864
33. Martinez MJ, Roy S, Archuletta AB, Wentzell PD, Anna-Arriola SS, Rodriguez AL, Aragon AD, Quiñones GA, Allen C, Werner-Washburne M (**2004**). Genomic analysis of stationary-phase and exit in Saccharomyces cerevisiae: gene expression and identification of novel essential genes. **Mol Biol Cell** 15 (12): 5295–5305. doi:10.1091/mbc.E03-11-0856
34. Erasmus DJ, Van Der Merwe GK, Van Vuuren HJJ (**2003**). Genome-wide expression analyses: Metabolic adaptation of Saccharomyces cerevisiae to high sugar stress. **FEMS Yeast Res** 3 (4): 375–399. doi:10.1016/S1567-1356(02)00203-9
35. Cohen BA, Pilpel Y, Mitra RD, Church GM (**2002**). Discrimination between Paralogs using Microarray Analysis: Application to the Yap1p and Yap2p Transcriptional Networks. **Mol Biol Cell** 13 (5): 1608–1614. doi:10.1091/mbc.01-10-0472
36. Venters BJ, Wachi S, Mavrich TN, Andersen BE, Jena P, Sinnamon AJ, Jain P, Rolleri NS, Jiang C, Hemeryck-Walsh C, Pugh BF (**2011**). A Comprehensive Genomic Binding Map of Gene and Chromatin Regulatory Proteins in Saccharomyces. **Mol Cell** 41 (4): 480–492. doi:10.1016/j.molcel.2011.01.015
37. Frey AG, Eide DJ (**2011**). Roles of Two Activation Domains in Zap1 in the Response to Zinc Deficiency in Saccharomyces cerevisiae. **Journal of Biological Chemistry** 286 (8): 6844–6854. doi:10.1074/jbc.M110.203927
38. Lyons TJ, Gasch AP, Gaither LA, Botstein D, Brown PO, Eide DJ (**2000**). Genome-wide characterization of the Zap1p zinc-responsive regulon in yeast. **Proceedings of the National Academy of Sciences** 97 (14): 7957–7962. doi:10.1073/pnas.97.14.7957
39. Feng Y, Zhang Y, Li J, Omran RP, Whiteway M, Feng J (**2022**). Transcriptional Profiling of the Candida albicans Response to the DNA Damage Agent Methyl Methanesulfonate. **Int J Mol Sci** 23 (14): 7555. doi:10.3390/ijms23147555
40. Wang J, Gao W, Tang X, Feng J (**2025**). Moh1 coordinates ROS-dependent apoptosis in genotoxic stress response of Candida albicans. **Fungal Biol** 129 (6): 101642. doi:10.1016/j.funbio.2025.101642
41. Lupas AN, Zhu H, Korycinski M (**2015**). The Thalidomide-Binding Domain of Cereblon Defines the CULT Domain Family and Is a New Member of the β-Tent Fold. **PLoS Comput Biol** 11 (1): e1004023. doi:10.1371/journal.pcbi.1004023
42. Stellfox ME, Nardi IK, Knippler CM, Foltz DR (**2016**). Differential Binding Partners of the Mis18α/β YIPPEE Domains Regulate Mis18 Complex Recruitment to Centromeres. **Cell Rep** 15 (10): 2127–2135. doi:10.1016/j.celrep.2016.05.004
43. Waterhouse AM, Procter JB, Martin DMA, Clamp M, Barton GJ (**2009**). Jalview Version 2—a multiple sequence alignment editor and analysis workbench. **Bioinformatics** 25 (9): 1189–1191. doi:10.1093/bioinformatics/btp033
44. Sievers F, Higgins DG (**2021**). The Clustal Omega Multiple Alignment Package. **Methods Mol Biol** 2231: 3–16. doi:10.1007/978-1-0716-1036-7_1
45. Drozdetskiy A, Cole C, Procter J, Barton GJ (**2015**). JPred4: a protein secondary structure prediction server. **Nucleic Acids Res** 43 (W1): W389–W394. doi:10.1093/nar/gkv332
46. Jumper J, et al. (**2021**). Highly accurate protein structure prediction with AlphaFold. **Nature** 596 (7873): 583–589. doi:10.1038/s41586-021-03819-2
47. Varadi M, Anyango S, Deshpande M, Nair S, Natassia C, Yordanova G, Yuan D, Stroe O, Wood G, Laydon A, Žídek A, Green T, Tunyasuvunakool K, Petersen S, Jumper J, Clancy E, Green R, Vora A, Lutfi M, Figurnov M, Cowie A, Hobbs N, Kohli P, Kleywegt G, Birney E, Hassabis D, Velankar S (**2022**). AlphaFold Protein Structure Database: massively expanding the structural coverage of protein-sequence space with high-accuracy models. **Nucleic Acids Res** 50 (D1): D439–D444. doi:10.1093/nar/gkab1061
48. Goddard TD, Huang CC, Meng EC, Pettersen EF, Couch GS, Morris JH, Ferrin TE (**2018**). UCSF ChimeraX: Meeting modern challenges in visualization and analysis. **Protein Sci** 27 (1): 14–25. doi:10.1002/pro.3235
49. Pettersen EF, Goddard TD, Huang CC, Meng EC, Couch GS, Croll TI, Morris JH, Ferrin TE (**2021**). UCSF ChimeraX: Structure visualization for researchers, educators, and developers. **Protein Sci** 30 (1): 70–82. doi:10.1002/pro.3943
50. Kelley LA, Mezulis S, Yates CM, Wass MN, Sternberg MJE (**2015**). The Phyre2 web portal for protein modeling, prediction and analysis. **Nat Protoc** 10 (6): 845–858. doi:10.1038/nprot.2015.053
51. Matyskiela ME, Clayton T, Zheng X, Mayne C, Tran E, Carpenter A, Pagarigan B, McDonald J, Rolfe M, Hamann LG, Lu G, Chamberlain PP (**2020**). Crystal structure of the SALL4–pomalidomide–cereblon–DDB1 complex. **Nat Struct Mol Biol** 27 (4): 319–322. doi:10.1038/s41594-020-0405-9
52. Kim HK, Ko TH, Nyamaa B, Lee SR, Kim N, Ko KS, Rhee BD, Park C-S, Nilius B, Han J (**2016**). Cereblon in health and disease. **Pflugers Arch** 468 (8): 1299–1309. doi:10.1007/s00424-016-1854-1
53. Lee KM, Yang S-J, Park S, Choi YD, Shin HK, Pak JH, Park C-S, Kim I (**2015**). Depletion of the cereblon gene activates the unfolded protein response and protects cells from ER stress-induced cell death. **Biochem Biophys Res Commun** 458 (1): 34–39. doi:10.1016/j.bbrc.2015.01.054
54. Subramanian L, Medina-Pritchard B, Barton R, Spiller F, Kulasegaran-Shylini R, Radaviciute G, Allshire RC, Arockia Jeyaprakash A (**2016**). Centromere localization and function of Mis18 requires Yippee-like domain-mediated oligomerization. **EMBO Rep** 17 (4): 496–507. doi:10.15252/embr.201541520
55. Fujita Y, Hayashi T, Kiyomitsu T, Toyoda Y, Kokubu A, Obuse C, Yanagida M (**2007**). Priming of Centromere for CENP-A Recruitment by Human hMis18α, hMis18β, and M18BP1. **Dev Cell** 12 (1): 17–30. doi:10.1016/j.devcel.2006.11.002
56. Fitzgerald ME, Vela A, Pyle AM (**2014**). Dicer-related helicase 3 forms an obligate dimer for recognizing 22G-RNA. **Nucleic Acids Res** 42 (6): 3919–3930. doi:10.1093/nar/gkt1383
57. Gu W, Shirayama M, Conte D, Vasale J, Batista PJ, Claycomb JM, Moresco JJ, Youngman EM, Keys J, Stoltz MJ, Chen C-CG, Chaves DA, Duan S, Kasschau KD, Fahlgren N, Yates JR, Mitani S, Carrington JC, Mello CC (**2009**). Distinct Argonaute-Mediated 22G-RNA Pathways Direct Genome Surveillance in the C. elegans Germline. **Mol Cell** 36 (2): 231–244. doi:10.1016/j.molcel.2009.09.020
58. Kim H-Y, Gladyshev VN (**2004**). Methionine Sulfoxide Reduction in Mammals: Characterization of Methionine-*R*-Sulfoxide Reductases. **Mol Biol Cell** 15 (3): 1055–1064. doi:10.1091/mbc.e03-08-0629
59. Koc A, Gladyshev VN (**2007**). Methionine Sulfoxide Reduction and the Aging Process. **Ann N Y Acad Sci** 1100 (1): 383–386. doi:10.1196/annals.1395.042
60. Hitchen PG, Prior JL, Oyston PCF, Panico M, Wren BW, Titball RW, Morris HR, Dell A (**2002**). Structural characterization of lipo-oligosaccharide (LOS) from *Yersinia pestis*: regulation of LOS structure by the PhoPQ system. **Mol Microbiol** 44 (6): 1637–1650. doi:10.1046/j.1365-2958.2002.02990.x
61. Broach JR (**2012**). Nutritional control of growth and development in yeast. **Genetics** 192 (1): 73–105. doi:10.1534/genetics.111.135731
62. Guaragnella N, Bettiga M (**2021**). Acetic acid stress in budding yeast: From molecular mechanisms to applications. **Yeast** 38 (7): 391–400. doi:10.1002/yea.3651
63. De Melo HF, Bonini BM, Thevelein J, Simões DA, Morais MA (**2010**). Physiological and molecular analysis of the stress response of *Saccharomyces cerevisiae* imposed by strong inorganic acid with implication to industrial fermentations. **J Appl Microbiol** 109 (1): 116–127. doi:10.1111/j.1365-2672.2009.04633.x

64. Betlej G, Bator E, Oklejewicz B, Potocki L, Górka A, Slowik-Borowiec M, Czarny W, Domka W, Kwiatkowska A (**2020**). Long-Term Adaption to High Osmotic Stress as a Tool for Improving Enological Characteristics in Industrial Wine Yeast. **Genes** 11 (5): 576. doi:10.3390/genes11050576

65. Duncan HM, Mackler B (**1966**). Electron Transport Systems of Yeast. **J Biol Chem** 241 (8): 1694–1697. doi:10.1016/S0021-9258(18)96691-3

66. Collinson LP, Dawes IW (**1992**). Inducibility of the response of yeast cells to peroxide stress. **J Gen Microbiol** 138 (2): 329–335. doi:10.1099/00221287-138-2-329

67. Herrero YR, Camas KL, Ullah A (**2023**). Characterization of biobased materials, in: Advanced Applications of Biobased Materials, Elsevier, pp. 111–143

68. Tang S-Y, Zhang W, Soffe R, Nahavandi S, Shukla R, Khoshmanesh K (**2014**). High Resolution Scanning Electron Microscopy of Cells Using Dielectrophoresis. **PLoS One** 9 (8): e104109. doi:10.1371/journal.pone.0104109

69. Navarro-Aviño JP, Prasad R, Miralles VJ, Benito RM, Serrano R (**1999**). A proposal for nomenclature of aldehyde dehydrogenases inSaccharomyces cerevisiae and characterization of the stress-inducibleALD2 andALD3 genes. **Yeast** 15 (10A): 829–842. doi:10.1002/(SICI)1097-0061(199907)15:10A<829::AID-YEA423>3.0.CO;2-9

70. White WH, Skatrud PL, Xue Z, Toyn JH (**2003**). Specialization of Function Among Aldehyde Dehydrogenases: The *ALD2* and *ALD3* Genes Are Required for *β*-Alanine Biosynthesis in *Saccharomyces cerevisiae*. **Genetics** 163 (1): 69–77. doi:10.1093/genetics/163.1.69

71. Hagen I, Ecker M, Lagorce A, Francois JM, Sestak S, Rachel R, Grossmann G, Hauser NC, Hoheisel JD, Tanner W, Strahl S (**2004**). Sed1p and Srl1p are required to compensate for cell wall instability in *Saccharomyces cerevisiae* mutants defective in multiple GPI-anchored mannoproteins. **Mol Microbiol** 52 (5): 1413–1425. doi:10.1111/j.1365-2958.2004.04064.x

72. Zhou Y, Zhou B, Pache L, Chang M, Khodabakhshi AH, Tanaseichuk O, Benner C, Chanda SK (**2019**). Metascape provides a biologist-oriented resource for the analysis of systems-level datasets. **Nat Commun** 10 (1): 1523. doi:10.1038/s41467-019-09234-6

73. Szklarczyk D, Gable AL, Lyon D, Junge A, Wyder S, Huerta-Cepas J, Simonovic M, Doncheva NT, Morris JH, Bork P, Jensen LJ, von Mering C (**2019**). STRING v11: protein–protein association networks with increased coverage, supporting functional discovery in genome-wide experimental datasets. **Nucleic Acids Res** 47 (D1): D607–D613. doi:10.1093/nar/gky1131

74. Liu H, Zhang J, Wang L, Liu H, Yu C, Li H (**2024**). Regulation of the RCK1 gene on the oxidative tolerance of Saccharomyces cerevisiae. **Free Radic Biol Med** 225: 15–23. doi:10.1016/j.freeradbiomed.2024.09.040

75. Fujita A, Hiroko T, Hiroko F, Oka C (**2005**). Enhancement of superficial pseudohyphal growth by overexpression of the SFG1 gene in yeast Saccharomyces cerevisiae. **Gene** 363: 97–104. doi:10.1016/j.gene.2005.06.036

76. Vandermeulen MD, Cullen PJ (**2020**). New Aspects of Invasive Growth Regulation Identified by Functional Profiling of MAPK Pathway Targets in *Saccharomyces cerevisiae*. **Genetics** 216 (1): 95–116. doi:10.1534/genetics.120.303369

77. Knözinger E (**1986**). P.R. Griffiths, J.A. de Haseth: Fourier Transform Infrared Spectroscopy, Vol. 83 aus der Reihe: Chemical Analysis—A Series of Monographs of Analytical Chemistry and Its Applications, John Wiley + Sons, Chichester, New York, Brisbane, Toronto, Singapore 1986. 656 Seiten. **Berichte der Bunsengesellschaft für physikalische Chemie** 90 (12): 1240–1241. doi:10.1002/bbpc.19860901224

78. Erukhimovitch V, Karpasasa M, Huleihel M (**2009**). Spectroscopic detection and identification of infected cells with herpes viruses. **Biopolymers** 91 (1): 61–67. doi:10.1002/bip.21082

79. Lasch P, Kneipp J (**2008**). Biomedical Vibrational Spectroscopy, Wiley, doi:10.1002/9780470283172

80. Taillandier E, Liquier J (**1992**). [16] Infrared spectroscopy of DNA. **Methods Enzymol** 211: 307–335. doi:10.1016/0076-6879(92)11018-e

81. Surewicz WK, Mantsch HH (**1988**). New insight into protein secondary structure from resolution-enhanced infrared spectra. **Biochim Biophys Acta** 952: 115–130. doi:10.1016/0167-4838(88)90107-0

82. Mantsch HH, McElhaney RN (**1991**). Phospholipid phase transitions in model and biological membranes as studied by infrared spectroscopy. **Chem Phys Lipids** 57 (2–3): 213–226. doi:10.1016/0009-3084(91)90077-O

83. Choo L, Jackson M, Halliday W, Mantsch H (**1993**). Infrared spectroscopic characterisation of multiple sclerosis plaques in the human central nervous system. **Biochim Biophys Acta** 1182 (3): 333–337. doi:10.1016/0925-4439(93)90078-F

84. Naumann D, Helm D, Labischinski H (**1991**). Microbiological characterizations by FT-IR spectroscopy. **Nature** 351 (6321): 81–82. doi:10.1038/351081a0

85. Helm D, Labischinski H, Schallehn G, Naumann D (**1991**). Classification and identification of bacteria by Fourier-transform infrared spectroscopy. **Microbiology** 137 (1): 69–79. doi:10.1099/00221287-137-1-69

86. Corte L, Rellini P, Roscini L, Fatichenti F, Cardinali G (**2010**). Development of a novel, FTIR (Fourier transform infrared spectroscopy) based, yeast bioassay for toxicity testing and stress response study. **Anal Chim Acta** 659 (1–2): 258–265. doi:10.1016/j.aca.2009.11.035

87. Mihoubi W, Sahli E, Gargouri A, Amiel C (**2017**). FTIR spectroscopy of whole cells for the monitoring of yeast apoptosis mediated by p53 overexpression and its suppression by Nigella sativa extracts. **PLoS One** 12 (7): e0180680. doi:10.1371/journal.pone.0180680

88. Taha M, Hassan M, Essa S, Tartor Y (**2013**). Use of Fourier transform infrared spectroscopy (FTIR) spectroscopy for rapid and accurate identification of Yeasts isolated from human and animals. **Int J Vet Sci Med** 1 (1): 15–20. doi:10.1016/j.ijvsm.2013.03.001

89. Shapaval V, Brandenburg J, Blomqvist J, Tafintseva V, Passoth V, Sandgren M, Kohler A (**2019**). Biochemical profiling, prediction of total lipid content and fatty acid profile in oleaginous yeasts by FTIR spectroscopy. **Biotechnol Biofuels** 12 (1): 140. doi:10.1186/s13068-019-1481-0

90. Kümmerle M, Scherer S, Seiler H (**1998**). Rapid and Reliable Identification of Food-Borne Yeasts by Fourier-Transform Infrared Spectroscopy. **Appl Environ Microbiol** 64 (6): 2207–2214. doi:10.1128/AEM.64.6.2207-2214.1998

91. Cavagna M, Dell'Anna R, Monti F, Rossi F, Torriani S (**2010**). Use of ATR-FTIR Microspectroscopy to Monitor Autolysis of *Saccharomyces cerevisiae* Cells in a Base Wine. **J Agric Food Chem** 58 (1): 39–45. doi:10.1021/jf902369s

92. Corte L, Antonielli L, Roscini L, Fatichenti F, Cardinali G (**2011**). Influence of cell parameters in Fourier transform infrared spectroscopy analysis of whole yeast cells. **Analyst** 136 (11): 2339. doi:10.1039/c0an00515k

93. Correa-García S, Bermúdez-Moretti M, Travo A, Déléris G, Forfar I (**2014**). FTIR spectroscopic metabolome analysis of lyophilized and fresh Saccharomyces cerevisiae yeast cells. **Analytical Methods** 6 (6): 1855. doi:10.1039/c3ay42322k

94. Shapaval V, Walczak B, Gognies S, Møretrø T, Suso HP, Wold Åsli A, Belarbi A, Kohler A (**2013**). FTIR spectroscopic characterization of differently cultivated food related yeasts. **Analyst** 138 (14): 4129. doi:10.1039/c3an00304c

95. Abdi H, Williams LJ (**2010**). Principal component analysis. **WIREs Computational Statistics** 2 (4): 433–459. doi:10.1002/wics.101

96. Grahn H, Szeverenyi NM, Roggenbuck MW, Delaglio F, Geladi P (**1989**). Data analysis of multivariate magnetic resonance images I. A principal component analysis approach. **Chemometrics and Intelligent Laboratory Systems** 5 (4): 311–322. doi:10.1016/0169-7439(89)80030-9

97. Beattie JR, Esmonde-White FWL (**2021**). Exploration of Principal Component Analysis: Deriving Principal Component Analysis Visually Using Spectra. **Appl Spectrosc** 75 (4): 361–375. doi:10.1177/0003702820987847

98. Cozzolino D, Power A, Chapman J (**2019**). Interpreting and Reporting Principal Component Analysis in Food Science Analysis and Beyond. **Food Anal Methods** 12 (11): 2469–2473. doi:10.1007/s12161-019-01605-5

99. Liu X, Renard CMGC, Bureau S, Le Bourvellec C (**2021**). Revisiting the contribution of ATR-FTIR spectroscopy to characterize plant cell wall polysaccharides. **Carbohydr Polym** 262: 117935. doi:10.1016/j.carbpol.2021.117935

100. Köhn H, Hubert LJ (**2015**). Hierarchical Cluster Analysis, in: Wiley StatsRef: Statistics Reference Online, Wiley, pub2, pp. 1–13. doi:10.1002/9781118445112.stat02449

101. Ernst R, Ejsing CS, Antonny B (**2016**). Homeoviscous Adaptation and the Regulation of Membrane Lipids. **J Mol Biol** 428 (24): 4776–4791. doi:10.1016/j.jmb.2016.08.013

102. Ferraz L, Sauer M, Sousa MJ, Branduardi P (**2021**). The Plasma Membrane at the Cornerstone Between Flexibility and Adaptability: Implications for Saccharomyces cerevisiae as a Cell Factory. **Front Microbiol** 12: 715891. doi:10.3389/fmicb.2021.715891

103. Klug L, Daum G (**2014**). Yeast lipid metabolism at a glance. **FEMS Yeast Res** 14 (3): 369–388. doi:10.1111/1567-1364.12141

104. Arrondo JLR, Muga A, Castresana J, Goñi FM (**1993**). Quantitative studies of the structure of proteins in solution by fourier-transform infrared spectroscopy. **Prog Biophys Mol Biol** 59 (1): 23–56. doi:10.1016/0079-6107(93)90006-6

105. Kong J, Yu S (**2007**). Fourier Transform Infrared Spectroscopic Analysis of Protein Secondary Structures. **Acta Biochim Biophys Sin** 39 (8): 549–559. doi:10.1111/j.1745-7270.2007.00320.x

106. Kassem A, Abbas L, Coutinho O, Opara S, Najaf H, Kasperek D, Pokhrel K, Li X, Tiquia-Arashiro S (**2023**). Applications of Fourier Transform-Infrared spectroscopy in microbial cell biology and environmental microbiology: advances, challenges, and future perspectives. **Front Microbiol** 14: 1304081. doi:10.3389/fmicb.2023.1304081

107. Reverter-Branchat G, Cabiscol E, Tamarit J, Ros J (**2004**). Oxidative Damage to Specific Proteins in Replicative and Chronological-aged Saccharomyces cerevisiae. **J Biol Chem** 279 (30): 31983–31989. doi:10.1074/jbc.M404849200

108. Fedorova M, Bollineni RC, Hoffmann R (**2014**). Protein carbonylation as a major hallmark of oxidative damage: Update of analytical strategies. **Mass Spectrom Rev** 33 (2): 79–97. doi:10.1002/mas.21381

109. Orlean P (**2012**). Architecture and Biosynthesis of the *Saccharomyces cerevisiae* Cell Wall. **Genetics** 192 (3): 775–818. doi:10.1534/genetics.112.144485

110. Klis FM, Mol P, Hellingwerf K, Brul S (**2002**). Dynamics of cell wall structure in *Saccharomyces cerevisiae*. **FEMS Microbiol Rev** 26 (3): 239–256. doi:10.1111/j.1574-6976.2002.tb00613.x

111. Ristow M, Schmeisser S (**2011**). Extending life span by increasing oxidative stress. **Free Radic Biol Med** 51 (2): 327–336. doi:10.1016/j.freeradbiomed.2011.05.010

112. Chelikani P, Fita I, Loewen PC (**2004**). Diversity of structures and properties among catalases. **Cell Mol Life Sci** 61 (2): 192–208. doi:10.1007/s00018-003-3206-5

113. Martins D, English AM (**2014**). Catalase activity is stimulated by H2O2 in rich culture medium and is required for H2O2 resistance and adaptation in yeast. **Redox Biol** 2: 308–313. doi:10.1016/j.redox.2013.12.019

114. Eruslanov E, Kusmartsev S (**2010**). Identification of ROS Using Oxidized DCFDA and Flow-Cytometry. **Methods Mol Biol** 594: 57–72. doi:10.1007/978-1-60761-411-1_4

115. Balaban RS, Nemoto S, Finkel T (**2005**). Mitochondria, Oxidants, and Aging. **Cell** 120 (4): 483–495. doi:10.1016/j.cell.2005.02.001

116. Bain JM, Louw J, Lewis LE, Okai B, Walls CA, Ballou ER, Walker LA, Reid D, Munro CA, Brown AJP, Brown GD, Gow NAR, Erwig LP (**2014**). Candida albicans Hypha Formation and Mannan Masking of β-Glucan Inhibit Macrophage Phagosome Maturation. **mBio** 5 (6): e01874. doi:10.1128/mBio.01874-14

117. Graus MS, Wester MJ, Lowman DW, Williams DL, Kruppa MD, Martinez CM, Young JM, Pappas HC, Lidke KA, Neumann AK (**2018**). Mannan Molecular Substructures Control Nanoscale Glucan Exposure in Candida. **Cell Rep** 24 (9): 2432–2442.e5. doi:10.1016/j.celrep.2018.07.088

118. Wheeler RT, Fink GR (**2006**). A Drug-Sensitive Genetic Network Masks Fungi from the Immune System. **PLoS Pathog** 2 (4): e35. doi:10.1371/journal.ppat.0020035

119. Levin DE (**2005**). Cell Wall Integrity Signaling in *Saccharomyces cerevisiae*. **Microbiol Mol Biol Rev** 69 (2): 262–291. doi:10.1128/MMBR.69.2.262-291.2005

120. Zhao F, Yang J, Li J, Li Z, Lin Y, Zheng S, Liang S, Han S (**2020**). Multiple cellular responses guarantee yeast survival in presence of the cell membrane/wall interfering agent sodium dodecyl sulfate. **Biochem Biophys Res Commun** 527 (1): 276–282. doi:10.1016/j.bbrc.2020.03.163

121. Lesage G, Bussey H (**2006**). Cell Wall Assembly in *Saccharomyces cerevisiae*. **Microbiol Mol Biol Rev** 70 (2): 317–343. doi:10.1128/MMBR.00038-05

122. Sousa-Lopes A, Antunes F, Cyrne L, Marinho HS (**2004**). Decreased cellular permeability to H_2O_2 protects *Saccharomyces cerevisiae* cells in stationary phase against oxidative stress. **FEBS Lett** 578 (1–2): 152–156. doi:10.1016/j.febslet.2004.10.090

123. Branco MR, Marinho HS, Cyrne L, Antunes F (**2004**). Decrease of H2O2 Plasma Membrane Permeability during Adaptation to H2O2 in Saccharomyces cerevisiae. **J Biol Chem** 279 (8): 6501–6506. doi:10.1074/jbc.M311818200

124. Semchyshyn HM, Abrat OB, Miedzobrodzki J, Inoue Y, Lushchak VI (**2011**). Acetate but not propionate induces oxidative stress in bakers' yeast *Saccharomyces cerevisiae*. **Redox Report** 16 (1): 15–23. doi:10.1179/174329211X12968219310954

125. Giannattasio S, Guaragnella N, Ždralević M, Marra E (**2013**). Molecular mechanisms of Saccharomyces cerevisiae stress adaptation and programmed cell death in response to acetic acid. **Front Microbiol** 4 (33). doi:10.3389/fmicb.2013.00033

126. Grimaud R, Ezraty B, Mitchell JK, Lafitte D, Briand C, Derrick PJ, Barras F (**2001**). Repair of Oxidized Proteins. **J Biol Chem** 276 (52): 48915–48920. doi:10.1074/jbc.M105509200

127. Moskovitz J, Bar-Noy S, Williams WM, Requena J, Berlett BS, Stadtman ER (**2001**). Methionine sulfoxide reductase (MsrA) is a regulator of antioxidant defense and lifespan in mammals. **Proc Natl Acad Sci U S A** 98 (23): 12920–12925. doi:10.1073/pnas.231472998

128. Kim IS, Lee M, Park KC, Jeon Y, Park JH, Hwang EJ, Jeon TI, Ko S, Lee H, Baek SH, Kim KI (**2012**). Roles of Mis18α in Epigenetic Regulation of Centromeric Chromatin and CENP-A Loading. **Mol Cell** 46 (3): 260–273. doi:10.1016/j.molcel.2012.03.021

129. Greene LH (**2012**). Protein structure networks. **Brief Funct Genomics** 11 (6): 469–478. doi:10.1093/bfgp/els039

130. De Las Rivas J, Fontanillo C (**2012**). Protein-protein interaction networks: unraveling the wiring of molecular machines within the cell. **Brief Funct Genomics** 11 (6): 489–496. doi:10.1093/bfgp/els036

131. Ho Y, et al. (**2002**). Systematic identification of protein complexes in Saccharomyces cerevisiae by mass spectrometry. **Nature** 415 (6868): 180–183. doi:10.1038/415180a

132. Smith TM, Willardson BM (**2022**). Mechanistic insights into protein folding by the eukaryotic chaperonin complex CCT. **Biochem Soc Trans** 50 (5): 1403–1414. doi:10.1042/BST20220591

133. Shen PS, Willardson BM (**2025**). Protein folding by the CCT/TRiC chaperone complex. **Curr Opin Struct Biol** 91: 102999. doi:10.1016/j.sbi.2025.102999

134. Narayanan A, Pullepu D, Kabir MA (**2016**). The interactome of CCT complex – A computational analysis. **Comput Biol Chem** 64: 396–402. doi:10.1016/j.compbiolchem.2016.09.002

135. Liu H, Pfirrmann T (**2019**). The Gid-complex: an emerging player in the ubiquitin ligase league. **Biol Chem** 400 (11): 1429–1441. doi:10.1515/hsz-2019-0139

136. Melnykov A, Chen S-J, Varshavsky A (**2019**). Gid10 as an alternative N-recognin of the Pro/N-degron pathway. **Proc Natl Acad Sci U S A** 116 (32): 15914–15923. doi:10.1073/pnas.1908304116

137. Kong K-YE, Fischer B, Meurer M, Kats I, Li Z, Rühle F, Barry JD, Kirrmaier D, Chevyreva V, San Luis B-J, Costanzo M, Huber W, Andrews BJ, Boone C, Knop M, Khmelinskii A (**2021**). Timer-based proteomic profiling of the ubiquitin-proteasome system reveals a substrate receptor of the GID ubiquitin ligase. **Mol Cell** 81 (11): 2460–2476.e11. doi:10.1016/j.molcel.2021.04.018

138. Chrustowicz J, Sherpa D, Teyra J, Loke MS, Popowicz GM, Basquin J, Sattler M, Prabu JR, Sidhu SS, Schulman BA (**2022**). Multifaceted N-Degron Recognition and Ubiquitylation by GID/CTLH E3 Ligases. **J Mol Biol** 434 (2): 167347. doi:10.1016/j.jmb.2021.167347

139. Santt O, Pfirrmann T, Braun B, Juretschke J, Kimmig P, Scheel H, Hofmann K, Thumm M, Wolf DH (**2008**). The Yeast GID Complex, a Novel Ubiquitin Ligase (E3) Involved in the Regulation of Carbohydrate Metabolism. **Mol Biol Cell** 19 (8): 3323–3333. doi:10.1091/mbc.e08-03-0328

140. Yan C, Fan M, Yang M, Zhao J, Zhang W, Su Y, Xiao L, Deng H, Xie D (**2018**). Injury Activates Ca2+/Calmodulin-Dependent Phosphorylation of JAV1-JAZ8-WRKY51 Complex for Jasmonate Biosynthesis. **Mol Cell** 70 (1): 136–149.e7. doi:10.1016/j.molcel.2018.03.013

141. Chen S-J, Wu X, Wadas B, Oh J-H, Varshavsky A (**2017**). An N-end rule pathway that recognizes proline and destroys gluconeogenic enzymes. **Science** 355 (6323): eaal3655. doi:10.1126/science.aal3655

142. Langlois CR, Beier V, Karayel O, Chrustowicz J, Sherpa D, Mann M, Schulman BA (**2022**). A GID E3 ligase assembly ubiquitinates an Rsp5 E3 adaptor and regulates plasma membrane transporters. **EMBO Rep** 23 (6). doi:10.15252/embr.202153835

143. Hepowit NL, Moon B, Ebert AC, Dickson RC, MacGurn JA (**2023**). Art2 mediates selective endocytosis of methionine transporters during adaptation to sphingolipid depletion. **J Cell Sci** 136 (14). jcs260675. doi:10.1242/jcs.260675

144. Lanz MC, Yugandhar K, Gupta S, Sanford EJ, Faça VM, Vega S, Joiner AMN, Fromme JC, Yu H, Smolka MB (**2021**). In-depth and 3-dimensional exploration of the budding yeast phosphoproteome. **EMBO Rep** 22 (2): e51121. doi:10.15252/embr.202051121

145. Boeke JD, La Croute F, Fink GR (**1984**). A positive selection for mutants lacking orotidine-5′-phosphate decarboxylase activity in yeast: 5-fluoro-orotic acid resistance. **Mol Gen Genet** 197 (2): 345–346. doi:10.1007/BF00330984

146. Livak KJ, Schmittgen TD (**2001**). Analysis of Relative Gene Expression Data Using Real-Time Quantitative PCR and the $2^{-\Delta\Delta CT}$ Method. **Methods** 25 (4): 402–408. doi:10.1006/meth.2001.1262

147. Bustin SA, Benes V, Garson JA, Hellemans J, Huggett J, Kubista M, Mueller R, Nolan T, Pfaffl MW, Shipley GL, Vandesompele J, Wittwer CT (**2009**). The MIQE Guidelines: Minimum Information for Publication of Quantitative Real-Time PCR Experiments. **Clin Chem** 55 (4): 611–622. doi:10.1373/clinchem.2008.112797

148. Huang J, Liang X, Xuan Y, Geng C, Li Y, Lu H, Qu S, Mei X, Chen H, Yu T, Sun N, Rao J, Wang J, Zhang W, Chen Y, Liao S, Jiang H, Liu X, Yang Z, Mu F, Gao S (**2018**). Erratum to: A reference human genome dataset of the BGISEQ-500 sequencer. **Gigascience** 7 (12). giy144. doi:10.1093/gigascience/giy144

149. Huang J, Liang X, Xuan Y, Geng C, Li Y, Lu H, Qu S, Mei X, Chen H, Yu T, Sun N, Rao J, Wang J, Zhang W, Chen Y, Liao S, Jiang H, Liu X, Yang Z, Mu F, Gao S (**2017**). A reference human genome dataset of the BGISEQ-500 sequencer. **Gigascience** 6 (5): 1–9. doi:10.1093/gigascience/gix024

150. Dobin A, Davis CA, Schlesinger F, Drenkow J, Zaleski C, Jha S, Batut P, Chaisson M, Gingeras TR (**2013**). STAR: ultrafast universal RNA-seq aligner. **Bioinformatics** 29 (1): 15–21. doi:10.1093/bioinformatics/bts635

151. Liao Y, Smyth GK, Shi W (**2014**). FeatureCounts: an efficient general purpose program for assigning sequence reads to genomic features. **Bioinformatics** 30 (7): 923–930. doi:10.1093/bioinformatics/btt656

152. Bozkurt O, Severcan M, Severcan F (**2010**). Diabetes induces compositional, Structural and functional alterations on rat skeletal soleus muscle revealed by FTIR spectroscopy: a comparative study with EDL muscle. **Analyst** 135 (12): 3110. doi:10.1039/c0an00542h

153. Kucuk Baloglu F, Guldag Tas D, Yilmaz O, Severcan F (**2023**). The recovery effect of Vitamin C on structural alterations due to Streptozotocin-Induced diabetes in rat testicular tissues. **Spectrochim Acta A Mol Biomol Spectrosc** 288: 122149. doi:10.1016/j.saa.2022.122149

154. Adochitei A, Drochioiu G (**2011**). Rapid Characterization of peptide secondary structure by FT-IR spectroscopy. **Revue Roumaine de Chimie** 56 (7): 783–791

155. Goormaghtigh E, Ruysschaert J-M, Raussens V (**2006**). Evaluation of the Information Content in Infrared Spectra for Protein Secondary Structure Determination. **Biophys J** 90 (8): 2946–2957. doi:10.1529/biophysj.105.072017

SUPPLEMENTAL REFERENCES

156. Shapira M, Segal E, Botstein D (**2004**). Disruption of Yeast Forkhead-associated Cell Cycle Transcription by Oxidative Stress. **Mol Biol Cell** 15 (12): 5659–5669. doi:10.1091/mbc.e04-04-0340

157. Haugen AC, Kelley R, Collins JB, Tucker CJ, Deng C, Afshari CA, Brown JM, Ideker T, Van Houten B (**2004**). Integrating phenotypic and expression profiles to map arsenic-response networks. **Genome Biol** 5 (12). R95. doi:10.1186/gb-2004-5-12-r95

158. Caba E, Dickinson DA, Warnes GR, Aubrecht J (**2005**). Differentiating mechanisms of toxicity using global gene expression analysis in Saccharomyces cerevisiae. **Mutat Res** 575 (1–2): 34–46. doi:10.1016/j.mrfmmm.2005.02.005

159. Thorsen M, Lagniel G, Kristiansson E, Junot C, Nerman O, Labarre J, Tamás MJ (**2007**). Quantitative transcriptome, proteome, and sulfur metabolite profiling of the *Saccharomyces cerevisiae* response to arsenite. **Physiol Genomics** 30 (1): 35–43. doi:10.1152/physiolgenomics.00236.2006

160. Shivaswamy S, Iyer VR (**2008**). Stress-Dependent Dynamics of Global Chromatin Remodeling in Yeast: Dual Role for SWI/SNF in the Heat Shock Stress Response. **Mol Cell Biol** 28 (7): 2221–2234. doi:10.1128/MCB.01659-07

161. O'Rourke SM, Herskowitz I (**2004**). Unique and Redundant Roles for HOG MAPK Pathway Components as Revealed by Whole-Genome Expression Analysis. **Mol Biol Cell** 15 (2): 532–542. doi:10.1091/mbc.e03-07-0521

162. Guan Q, Haroon S, Bravo DG, Will JL, Gasch AP (**2012**). Cellular Memory of Acquired Stress Resistance in *Saccharomyces cerevisiae*. **Genetics** 192 (2): 495–505. doi:10.1534/genetics.112.143016

163. Gomar-Alba M, Morcillo-Parra MÁ, Olmo M del (**2015**). Response of yeast cells to high glucose involves molecular and physiological differences when compared to other osmostress conditions. **FEMS Yeast Res** 15 (5): fov039. doi:10.1093/femsyr/fov039

164. Oeser ML, Amen T, Nadel CM, Bradley AI, Reed BJ, Jones RD, Gopalan J, Kaganovich D, Gardner RG (**2016**). Dynamic Sumoylation of a Conserved Transcription Corepressor Prevents Persistent Inclusion Formation during Hyperosmotic Stress. **PLoS Genet** 12 (1): e1005809. doi:10.1371/journal.pgen.1005809

165. Fry RC, Sambandan TG, Rha C (**2003**). DNA damage and stress transcripts in *Saccharomyces cerevisiae* Mutant sgs1. **Mech Ageing Dev** 124 (7): 839–846. doi:10.1016/S0047-6374(03)00144-1

166. Wu C-Y, Bird AJ, Chung LM, Newton MA, Winge DR, Eide DJ (**2008**). Differential control of Zap1-regulated genes in response to zinc deficiency in Saccharomyces cerevisiae. **BMC Genomics** 9 (1): 370. doi:10.1186/1471-2164-9-370

167. Moreno-Cermeño A, Alsina D, Cabiscol E, Tamarit J, Ros J (**2013**). Metabolic remodeling in frataxin-deficient yeast is mediated by Cth2 and Adr1. **Biochim Biophys Acta** 1833 (12): 3326–3337. doi:10.1016/j.bbamcr.2013.09.019

168. Tyo KE, Liu Z, Petranovic D, Nielsen J (**2012**). Imbalance of heterologous protein folding and disulfide bond formation rates yields runaway oxidative stress. **BMC Biol** 10 (1): 16. doi:10.1186/1741-7007-10-16

169. Dubacq C, Chevalier A, Courbeyrette R, Petat C, Gidrol X, Mann C (**2006**). **Mol Genet Genomics** 275 (2): 114–124. doi:10.1007/s00438-005-0077-5

170. Aragon AD, Quiñones GA, Thomas EV, Roy S, Werner-Washburne M (**2006**). Release of extraction-resistant mRNA in stationary phase Saccharomyces cerevisiae produces a massive increase in transcript abundance in response to stress. **Genome Biol** 7 (2): R9. doi:10.1186/gb-2006-7-2-r9

171. Tsang CK, Liu Y, Thomas J, Zhang Y, Zheng XFS (**2014**). Superoxide dismutase 1 acts as a nuclear transcription factor to regulate oxidative stress resistance. **Nat Commun** 5 (1): 3446. doi:10.1038/ncomms4446

172. S Puig, Vergara SV, Thiele DJ (**2008**). Cooperation of Two mRNA-Binding Proteins Drives Metabolic Adaptation to Iron Deficiency. **Cell Metab** 7 (6): 555–564. doi:10.1016/j.cmet.2008.04.010

173. Pastor-Flores D, Ferrer-Dalmau J, Bahí A, Boleda M, Biondi RM, Casamayor A (**2015**). Depletion of yeast PDK1 orthologs triggers a stress-like transcriptional response. **BMC Genomics** 16 (1): 719. doi:10.1186/s12864-015-1903-8

174. Capaldi AP, Kaplan T, Liu Y, Habib N, Regev A, Friedman N, O'Shea EK (**2008**). Structure and function of a transcriptional network activated by the MAPK Hog1. **Nat Genet** 40 (11): 1300–1306. doi:10.1038/ng.235

175. Gross C, Kelleher M, Iyer VR, Brown PO, Winge DR (**2000**). Identification of the Copper Regulon in Saccharomyces cerevisiae by DNA Microarrays. **J Biol Chem** 275 (41): 32310–32316. doi:10.1074/jbc.M005946200

176. Berry DB, Gasch AP (**2008**). Stress-activated Genomic Expression Changes Serve a Preparative Role for Impending Stress in Yeast. **Mol Biol Cell** 19 (11): 4580–4587. doi:10.1091/mbc.e07-07-0680

177. Willis IM, Chua G, Tong AH, Brost RL, Hughes TR, Boone C, Moir RD (**2008**). Genetic Interactions of MAF1 Identify a Role for Med20 in Transcriptional Repression of Ribosomal Protein Genes. **PLoS Genet** 4 (7): e1000112. doi:10.1371/journal.pgen.1000112

178. Gasch AP, Spellman PT, Kao CM, Carmel-Harel O, Eisen MB, Storz G, Botstein D, Brown PO (**2000**). Genomic Expression Programs in the Response of Yeast Cells to Environmental Changes. **Mol Biol Cell** 11 (12): 4241–4257. doi:10.1091/mbc.11.12.4241

179. Yamamoto A, Mizukami Y, Sakurai H (**2005**). Identification of a Novel Class of Target Genes and a Novel Type of Binding Sequence of Heat Shock Transcription Factor in Saccharomyces cerevisiae. **J Biol Chem** 280 (12): 11911–11919. doi:10.1074/jbc.M411256200

180. Navlakha S, Gitter A, Bar-Joseph Z (**2012**). A Network-based Approach for Predicting Missing Pathway Interactions. **PLoS Comput Biol** 8 (8): e1002640. doi:10.1371/journal.pcbi.1002640

181. Chasman D, Ho Y, Berry DB, Nemec CM, MacGilvray ME, Hose J, Merrill AE, Lee MV, Will JL, Coon JJ, Ansari AZ, Craven M, Gasch AP (**2014**). Pathway connectivity and signaling coordination in the yeast stress-activated signaling network. **Mol Syst Biol** 10 (11): 759. doi:10.15252/msb.20145120

182. Causton HC, Ren B, Koh SS, Harbison CT, Kanin E, Jennings EG, Lee TI, True HL, Lander ES, Young RA (**2001**). Remodeling of Yeast Genome Expression in Response to Environmental Changes. **Mol Biol Cell** 12 (2): 323–337. doi:10.1091/mbc.12.2.323

183. Lewis JA, Broman AT, Will J, Gasch AP (**2014**). Genetic Architecture of Ethanol-Responsive Transcriptome Variation in *Saccharomyces cerevisiae* Strains. **Genetics** 198 (1): 369–382. doi:10.1534/genetics.114.167429

184. Segal E, Shapira M, Regev A, Pe'er D, Botstein D, Koller D, Friedman N (**2003**). Module networks: identifying regulatory modules and their condition-specific regulators from gene expression data. **Nat Genet** 34 (2): 166–176. doi:10.1038/ng1165

185. Shalem O, Groisman B, Choder M, Dahan O, Pilpel Y (**2011**). Transcriptome Kinetics Is Governed by a Genome-Wide Coupling of mRNA Production and Degradation: A Role for RNA Pol II. **PLoS Genet** 7 (9): e1002273. doi:10.1371/journal.pgen.1002273

186. Szeghalmi A, Kaminskyj S, Gough KM (**2007**). A synchrotron FTIR microspectroscopy investigation of fungal hyphae grown under optimal and stressed conditions. **Anal Bioanal Chem** 387 (5): 1779–1789. doi:10.1007/s00216-006-0850-2

187. Berterame NM, Porro D, Ami D, Branduardi P (**2016**). Protein aggregation and membrane lipid modifications under lactic acid stress in wild type and OPI1 deleted Saccharomyces cerevisiae strains. **Microb Cell Fact** 15 (1): 39. doi:10.1186/s12934-016-0438-2

188. Galichet A, Sockalingum GD, Belarbi A, Manfait M (**2001**). FTIR spectroscopic analysis of *Saccharomyces cerevisiae* cell walls: study of an anomalous strain exhibiting a pink-colored cell phenotype. **FEMS Microbiol Lett** 197 (2): 179–186. doi:10.1111/j.1574-6968.2001.tb10601.x

189. Bakir G, Dahms TES, Martin-Yken H, Bechtel HA, Gough KM (**2024**). *Saccharomyces cerevisiae* CellWall Remodeling in the Absence of Knr4 and Kre6 Revealed by Nano-FourierTransform Infrared Spectroscopy. **Appl Spectrosc** 78 (4): 355–364. doi:10.1177/00037028231213658